ESAIM: M2AN 53 (2019) 1433–1457
https://doi.org/10.1051/m2an/2019003

ESAIM: Mathematical Modelling and Numerical Analysis
www.esaim-m2an.org

A POSITIVITY-PRESERVING CENTRAL-UPWIND SCHEME FOR ISENTROPIC TWO-PHASE FLOWS THROUGH DEVIATED PIPES

Gerardo Hernandez-Duenas[1,*,**], Ulises Velasco-García[1,***]
and Jorge X. Velasco-Hernández[1,****]

Abstract. Directional drilling in oil and gas extraction can encounter difficulties such as accumulation of solids in deviated pipes. Motivated by such phenomenon, we consider a model for isentropic two-phase flows through deviated pipes. The system of partial differential equations is aimed at simulating the dynamics between a particle bed and a gas phase. The pipe can be either horizontal or vertically deviated where the effects of gravity are incorporated. Furthermore, the acceleration or deceleration due to friction between phases is investigated and spectral properties of the hyperbolic system of balance laws are described. The existence and characterization of steady states under appropriate conditions is analyzed. A new type of steady states arises when a balance between gas and solid phases results in a non-uniform solid particle bed and vanishing solid velocity. This state corresponds to an accumulation of sedimented solids. A central-upwind scheme that preserves the positivity of the gas and solid densities and volume fractions is presented. Including an application of the model to an analysis of accumulation of solids, a variety of numerical tests is presented to show the merits of the scheme.

Mathematics Subject Classification. 35L65, 65M08, 76T25.

Received June 8, 2018. Accepted January 11, 2019.

1. Introduction

Oil and gas extraction is one of the most important activities for our modern society. Mathematical and engineering methodologies have been developed in that direction since the very beginning of such activities. However, there is still the need to generate accurate, robust and efficient ways of solving mathematical models associated with multi-phase flows. In this paper we develop a relatively simple model for fluid flow in a pipe oriented to three scenarios. One of them is related to directional drilling. This technology uses deviated wells to increase production and optimally exploit a reservoir. We concentrate on gas flow associated to rock cuttings flowing in a deviated pipe and present results on bed formation, accumulation and transport. Another scenario is a more theoretical one and deals with Riemann problems in two-phase flows. We assume that somewhere

---

Keywords and phrases. Multiphase compressible flow, Riemann problems, Source terms, central-upwind schemes.

[1] Institute of Mathematics, National University of Mexico, Blvd. Juriquilla, 3001 Queretaro, Mexico.
[*] Corresponding author: `hernandez@im.unam.mx`

[**] Research was supported in part by grant UNAM-DGAPA-PAPIIT IA104517 (Investigación realizada gracias al programa UNAM-DGAPA-PAPIIT IA104517).
[***] Research was supported in part by grant UNAM-DGAPA-PAPIIT IN110917.
[****] Research was supported in part by Conacyt (FORDECyT) postdoctoral grant number 265667.

along the pipe a membrane initially separates the fluid into two regions with distinct densities and velocities. We are concerned here with the stability and robustness of the numerical method. The relevance of this theoretical scenario relies on the fact that two-phase flow problems require good numerical schemes if models are going to be of any use. Analysis of bed formation and cuttings transport in petroleum engineering represents our third scenario. To simplify the treatment of the model we assume that the fluid consists of a solid (rock cuttings) and a gas phase. Indeed, specially designed muds are used to remove cuttings [3, 31]. Our model uses a gas phase to exemplify the properties of our methods but its generalization to a viscous liquid phase requires further considerations to be presented in a future work. We however, intend to concentrate in the design of a robust numerical scheme and the solid-gas interactions lends itself nicely to this effect. An schematic of the model can be found in Figure 1.

One of the central problems of directional drilling is the production and accumulation of rock cuttings that can stuck and damage the drillstring [34]. For this reason the surveillance and frequent cleaning of boreholes is of utmost importance for the continuous production of a well. Wellbore cleaning operations have inherent difficulties since the removal of cuttings becomes a task that requires knowledge and control of a set of variables and parameters including cutting bed heights, wellbore configuration, fluid properties, cuttings characteristics, pipe eccentricity and rotary speed [30, 31]. Ultimately, cuttings are transported out of the well by special fluids (muds) and therefore knowledge of fluid regimes and dynamics in a pipe are necessary. Simplified gas-liquid two-phase flow models for drilling can be found in Flåtten *et al.* [13]. They assume an ideal gas law and an incompressible liquid phase for the equation of state. Furthermore, three different gas-liquid scenarios are considered and studied via numerical simulations. In Làrez-Vàzquez [24] a two-layer *mechanistic* model with two phases (liquid and solid) is proposed. One layer represents the sand bed at the bottom of the pipe which may be static while the other one at the top of the pipe is heterogeneous. It models the behaviour of sand particles during the wellbore cleaning with flexible pipes. The proposed model in Làrez-Vàzquez [24] considers a permanent regime, incompressible solid-liquid mix, constant flux density and constant rheological properties for the two phases, uniform particle distribution, no mass-exchange between liquid and solid phase, the height of the interfaces is constant on each section, among other considerations. In Làrez-Vàzquez [24], the main goal is the analysis of accumulation of solids in the pipe and critical velocities to avoid strong variations in the solid particles' bed.

Solids can accumulate in directional wells to form a stationary bed of cuttings occupying a section of the pipe's cross-sectional area [31, 44]. Mathematical models can help predicting such formations and their preferred locations subject to realistic conditions of fluid density, well inclination angle and solid volume fractions among others. Fluid velocity can impose different flow patterns within a pipe. High velocities induce a homogeneous suspension of cuttings being transported. Slightly lower velocities induce heterogeneous suspension. More moderate velocities generate a moving cuttings bed that coexists with a heterogeneous suspension of cuttings. Low velocities produce three layers consisting of a solid moving bed, a stationary solid bed and a heterogeneous suspension of cuttings [31]. Wells with inclinations (with respect to the vertical) greater than 5° are called directional wells while those with inclinations greater than 85° are called horizontal wells [12]. Deviation angles have a large influence in the formation of cutting beds and other transport phenomena [31]. It is clear that given enough fluid velocity all cuttings can be removed from a pipe. However, fluid velocity depends on pump capacity and surface and bottomhole dynamic pressures. Such conditions make unfeasible the straightforward solution of transporting cuttings out of the well.

A variety of models for two-phase flows are available in the literature. For instance, an approximate Riemann solver for the isentropic Baer-Nunziato two-phase flow model is constructed in Coquel *et al.* [8]. A relaxation approximation of the model is considered, providing exact solutions of the Riemann problem for subsonic relative speeds. A finite volume scheme on unstructured meshes is presented in Combe and Hérard [5] where a fractional step method is implemented. Approximate Roe-type Riemann solvers are used to calculate numerical convective fluxes. In Coquel *et al.* [6], a fractional step algorithm for computing approximate solutions of an isentropic Baer-Nunziato two-phase flow model is shown. The scheme relies on an operator splitting method corresponding to a different treatment of accelerated propagation phenomena originated from the acoustic waves

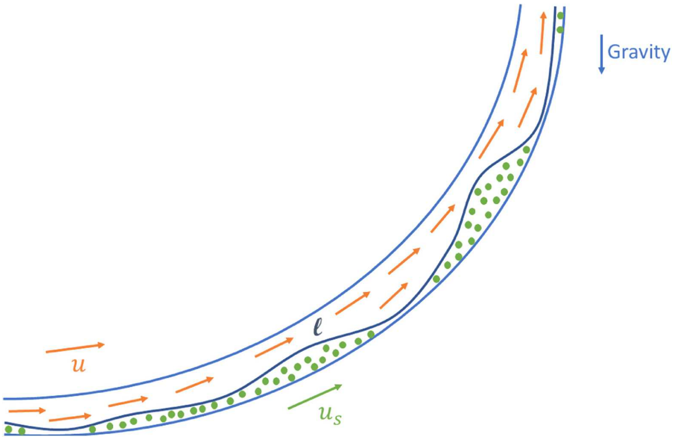

FIGURE 1. Illustration of a pipe geometry and the gas-solid flows.

on one hand and slow propagation phenomena due to the fluid motion on the other hand. The scheme preserves positive values of phase fractions and densities. In [38, 38, 40, 42, 43] the authors present Baer-Nunziato models for deflagration-to-detonation transition in granular materials. They include Lax-Friederich, Richtmyer-type and Roe-type numerical schemes with considerations of positivity of the volume fraction in both phases and well-balanced properties. In Thanh [39, 41] the existence of solutions of the Riemann problem for a model of two-phase flows is studied, while a well-balanced Godunov-type scheme for a model of a general fluid flow in a nozzle with variable cross-section is presented in Cuong and Thanh [9]. In Thanh [37] a class of exact solutions of a two-phase compressible flow model with and without gravity is considered. The equations in Thanh [37] form a non-hyperbolic system of balance laws and explicit expressions of the characteristic fields may not be available. This can represent an obstacle when solving Riemann problems. Interesting data is provided such as the Riemann invariants in the linearly degenerate characteristic fields and results related to the contact waves of the model without gravity are obtained. In García-Cascales *et al.* [14] numerical schemes are constructed to obtain approximate solutions to a system derived from the Baer-Nunziato model assuming multiphase mixtures of gas and particles with a solid incompressible phase. This model includes drag force, interfacial convective heat transfer, and interfacial exchange of mass, momentum and energy due to phase changes and chemical reactions among others.

In this work we present a mathematical isentropic Baer-Nunziato model and an efficient numerical scheme for a two-phase fluid through deviated pipes. Our motivation is the removal of cuttings out of a well but here we concentrate on the development of the model and, more importantly, on the design of an efficient numerical method that can deal with the difficulties that two-phase flow models may present. Effects of gravity and momentum exchange due to friction between phases are included. We focus on studying spectral properties of the model to determine the shock, rarefaction and compaction waves that might appear in a Riemann problem. We also investigate steady states that arise when there is a balance between pressure gradients and source terms and determine two classes of such equilibrium states. One of them has constant volume fraction in a way that the two phases evolve independently. Effects of gravity modify the invariants determining the steady states compared to regular Baer-Nunziato systems [29]. On the other hand, a new class of equilibrium states arises when non-uniform solid volume fractions can form as the solid velocity vanishes and the rest of the variables reach a balance. Although we did not consider steady states at rest in our numerical tests, we show a well-balanced property in the appendix. Such property recognizes steady sates at rest in the absence of a solid phase where the pressure gradients and gravity forces are in balance. Positivity preserving schemes have the desirable property that if the initial density and volume fractions are non-negative so is the numerical solution in subsequent steps. Such property provides enhanced stability when the density or the volume fraction are small. Here we construct a central-upwind scheme with that property.

This paper is organized as follows. In Section 2 an isentropic Baer-Nunziato type system for two phases in deviated pipes is presented where the coupling between phases occurs through changes in porosity. The main properties of the scheme are analyzed. Section 3 is devoted to the details of the numerical scheme and the proof of the positivity-preserving property. A set of numerical tests is presented in Section 4 to show the merits of the scheme. The numerical results include Riemann problems and a comparison with exact solutions to verify the convergence rate of the numerical scheme, convergence to steady states, a vacuum problem and a study of accumulation of solids in deviated pipes. Appendix A describes a well-balanced property that recognizes steady states at rest in the absence of a solid phase where pressure gradients are in balance with gravity forces. Appendix B shows how to compute exact solutions to the Riemann problem.

2. The model and its properties

The system here is an isentropic model for two-phase flows that we envision as gas and rock cuttings. The dynamics of the flow is dictated by conservation of mass and balance of momentum for both the solid and gas phases. The flow propagates in a deviated pipe and the effects of gravity are included, depending on the angle of the pipe. The momentum evolution also involves the friction of one phase on each other. The system reads

$$\begin{array}{lll}
\partial_t(\alpha\rho) & +\, \partial_\ell(\alpha\rho u) & = 0, \\
\partial_t(\alpha\rho u) & +\, \partial_\ell(\alpha(\rho u^2 + p)) & = -p\partial_\ell \alpha_s - g\alpha\rho\sin(\theta) + F_{dg}, \\
\partial_t(\alpha_s\rho_s) & +\, \partial_\ell(\alpha_s\rho_s u_s) & = 0, \\
\partial_t(\alpha_s\rho_s u_s) & +\, \partial_\ell(\alpha_s(\rho_s u_s^2 + p_s)) & = p\partial_\ell\alpha_s - g\alpha_s\rho_s\sin(\theta) - F_{dg}, \\
\partial_t\rho_s & +\, \partial_\ell(\rho_s u_s) & = 0, \quad \ell \in [a,b] \subset \mathbb{R},\ t > 0.
\end{array} \tag{2.1}$$

Here t is time and ℓ is the arclength of the deviated pipe (see Fig. 1). We note that we use the variable ℓ for arclength to avoid confusion with its horizontal coordinate x. The subindex s represents the solid phase and the absence of subindex stands for the gas phase. Furthermore, α, ρ, u and p denote the volume fraction, density, velocity and pressure respectively (and the equivalent description for the solid phase). Each subsystem is closed by assuming a barotropic fluid so that in each phase, the corresponding pressure is an explicit function of density

$$p = p(\rho),\ p(0) = 0,\ p_s = p_s(\rho_s),\ p_s(0) = 0,$$

satisfying $p'(\rho) > 0,\ p_s'(\rho_s)$ for $\rho,\ \rho_s > 0$. The speed of sound in each phase is defined as

$$c = \sqrt{p'(\rho)},\ c_s = \sqrt{p_s'(\rho_s)}.$$

Although the model is written for barotropic pressures in general, we will assume a perfect gas equation of state (PG EOS) for the gas phase and a stiffened gas equation of state (SG EOS) for the solid phase in the numerical experiments and in the description of steady states.

The first and third equations in (2.1) describe the conservation of mass in each phase; the second and the fourth equations describe the balance of momentum in each phase. The coupling between phases occurs through changes in porosity (α_s). The solid and gas volume fractions satisfy $\alpha + \alpha_s = 1$ and generate a momentum exchange between the two phases. The deviated pipe is assumed to form an angle $\theta(\ell)$ with respect to the surface (horizontal axis), at each arclength position ℓ in the pipe (here we depart from the convention in petroleum engineering to take the angle with respect to the vertical, not the horizontal axis). The acceleration of gravity is included and depends on the angle θ so that it is negligible in horizontal flows. The gravitational constant is $g = 9.81\,\mathrm{m\,s^{-2}}$. The last source term in the momentum equations represents the interfacial friction between phases [14]

$$F_{dg} = -\frac{3}{4}\frac{C_d}{d_p}\alpha_s\rho|u - u_s|(u - u_s).$$

Here the rate of momentum transfer towards the phase with the lowest velocity depends on the solution and is given by $\tau^{-1} = \frac{3}{4}\frac{C_d}{d_p}|u - u_s|$, where d_p is a reference value for the diameter of the solid particles, and C_d is a drag coefficient.

Hyperbolic balance laws with source terms that do not depend on derivatives of the solution does not modify the Rankine-Hugoniot jump conditions in weak solutions. However, system (2.1) consists of balance laws with non-conservative products. This adds both theoretical and numerical complications such as the concept of weak solutions. In Dal Maso *et al.* [10], a definition of weak solutions based on the theory of non-conservative products is provided and more on the theory of paths can be found in [25,26]. This theory allows us to construct solutions to the Riemann problem for two-phase flows. See Andrianov and Warnecke [2] for more details. Possible computational issues are analyzed in Abgrall and Karni [1].

We note that by recombining the third and fifth equations in (2.1), we get an equivalent equation (valid for smooth flows)

$$\partial_t \alpha_s + u_s \partial_\ell \alpha_s = 0, \tag{2.2}$$

which is not in conservation form. Although non-conservative products appear in system (2.1), we adopt the conservative form in the solid volume fraction because our numerical scheme strongly depends on the construction of numerical fluxes. In Coquel [7], a class of two-fluid two-phase flows is presented where the solid velocity in (2.2) is replaced by a weighted average between the solid and gas velocities. In Coquel [7] they also allow for an exchange of volume fraction, momentum and energy through pressure, velocity and temperature relaxation terms. In the present system (2.1), no mass or energy exchange is allowed, resulting in infinite relaxation timescales.

2.1. Quasilinear form

Important properties of the system such as hyperbolicity are clearly deduced from its quasilinear form. Furthermore, Roe-type numerical schemes require spectral information in their algorithms [15]. Central schemes require at least an estimation of the largest eigenvalue. The full spectral information is described in the following proposition.

Proposition 2.1. *System* (2.1) *can be written in quasilinear form as*

$$\begin{pmatrix} \alpha\rho \\ \alpha\rho u \\ \alpha_s\rho_s \\ \alpha_s\rho_s u_s \\ \rho_s \end{pmatrix}_t + \begin{pmatrix} 0 & 1 & 0 & 0 & 0 \\ c^2 - u^2 & 2u & \dfrac{\rho c^2}{\rho_s} & 0 & \dfrac{-\alpha_s \rho c^2}{\rho_s} \\ 0 & 0 & 0 & 1 & 0 \\ 0 & 0 & \dfrac{p_s - p}{\rho_s} - u_s^2 & 2u_s & \alpha_s\left(c_s^2 + \dfrac{p - p_s}{\rho_s}\right) \\ 0 & 0 & \dfrac{-u_s}{\alpha_s} & \dfrac{1}{\alpha_s} & u_s \end{pmatrix} \begin{pmatrix} \alpha\rho \\ \alpha\rho u \\ \alpha_s\rho_s \\ \alpha_s\rho_s u_s \\ \rho_s \end{pmatrix}_\ell = \begin{pmatrix} 0 \\ -g\alpha\rho\sin(\theta) + F_{dg} \\ 0 \\ -g\alpha_s\rho_s\sin(\theta) - F_{dg} \\ 0 \end{pmatrix}. \tag{2.3}$$

Furthermore, the eigenvalues of this system are given by the diagonal matrix $\Lambda = \mathrm{diag}(u - c,\ u + c,\ u_s,\ u_s - c_s,\ u_s + c_s)$*, with corresponding matrix of eigenvectors*

$$R = \begin{pmatrix} 1 & 1 & -\alpha_s(c_s c)^2\rho & 0 & 0 \\ u - c & u + c & -u_s\alpha_s(c_s c)^2\rho & 0 & 0 \\ 0 & 0 & \alpha_s(p - p_s + c_s^2\rho_s)(c^2 - v_g^2) & 1 & 1 \\ 0 & 0 & u_s\alpha_s(p - p_s + c_s^2\rho_s)(c^2 - v_g^2) & u_s - c_s & u_s + c_s \\ 0 & 0 & (p - p_s)(c^2 - v_g^2) & 1/\alpha_s & 1/\alpha_s \end{pmatrix}.$$

Here $v_g = u - u_s$ *is the gas velocity relative to the solid velocity. The system is conditionally hyperbolic, and looses hyperbolicity when one of the following conditions holds:* $\rho = 0,\ \rho_s = 0$ *or* $u_s = u \pm c$*.*

Let us recall that a characteristic field is said to be genuinely nonlinear if $\nabla\lambda_p(u)\cdot\mathbf{r}_p(u)\neq 0$ for all u. On the other hand, a field is linearly degenerate if it satisfies $\nabla\lambda_p(u)\cdot\mathbf{r}_p(u)\equiv 0$ for all u. Here λ_p denotes an eigenvalue and $\mathbf{r}_p$ denotes a corresponding eigenvector. See also [27,36] for more details. The first two characteristic fields are associated to the gas phase dynamics. Those two fields are genuinely non-linear (GNL) and can be either shock or rarefaction waves. Similarly, the last two characteristic families correspond to the solid phase and are also GNL. The third characteristic field with eigenvalue u_s is associated with the compaction wave due to jumps in porosity. This field is linearly degenerate (LD). Even though system (2.1) is not in conservation form, the above classification of the wave fields can be useful in the existence of weak solutions and uniqueness of jump conditions. Theoretical results are provided in [4,16] using probabilistic algorithms and a wave-front tracking method, respectively.

2.2. Steady states

The model can be applied to the analysis of accumulation of solids in a pipe. This phenomenon can occur when the system has reached a steady state. In the current model, steady state solutions occur when flux gradients are in balance with the source terms. Equilibrium solutions can appear in real-life test cases where the interfacial friction plays an important role. However, the absence of interfacial friction ($F_{dg}=0$) can help us characterize smooth steady-state flows and test the well-balanced property of our numerical scheme. Furthermore, we assume a PG EOS in the gas phase

$$p=\eta\left(\frac{\rho}{\rho_o}\right)^{\gamma}. \tag{2.4}$$

Here, $\rho_o = 1\,\mathrm{kg\,m^{-3}}$, the entropy η is constant in space and time and γ is the ratio of gas constants. A SG EOS is assumed in the solid phase, giving the relation

$$p_s+p_o=\eta_s\left(\frac{\rho_s}{\rho_o}\right)^{\gamma_s}. \tag{2.5}$$

Here the stiffening pressure p_o, solid entropy η_s and the polytropic exponent γ_s are assumed constant [2,35]. The corresponding gas and solid speeds of sound are

$$c=\sqrt{\frac{\gamma p}{\rho}}\ \text{and}\ c_s=\sqrt{\frac{\gamma_s(p_s+p_o)}{\rho_s}}, \tag{2.6}$$

respectively.

Conservation of mass in the solid phase immediately implies that either the solid velocity vanishes or the solid volume fraction is constant (decoupling the two sub-systems). Further details are given in the following proposition.

Proposition 2.2. *Let* $h=\frac{1}{2}u^2+\frac{c^2}{\gamma-1}$ *and* $h_s=\frac{1}{2}u_s^2+\frac{c_s^2}{\gamma_s-1}$ *be the gas and solid specific enthalpies respectively, and* $G(\ell)=g\int_{\ell_o}^{\ell}\sin(\theta(s))ds$ *the integrated vertical component of acceleration due to gravity. Smooth steady-state flows of system* (2.1) *in the absence of interfacial friction satisfy one of the following conditions:*

(i) The solid volume fraction α_s*, the solid and gas discharges* $Q=\alpha\rho u$, $Q_s=\alpha_s\rho_s u_s$ *and the quantities* $h+G$ *and* h_s+G *are all constant in space and time.*

(ii) Solid sedimentation. The solid velocity vanishes $u_s=0$*, the gas discharge* Q *and the quantity* $h+G$ *are constant in space and time, and the solid density satisfies the following ODE:*

$$\partial_\ell(\alpha_s p_s)=p\partial_\ell\alpha_s-g\alpha_s\rho_s\sin(\theta(\ell)). \tag{2.7}$$

Proof. Assume our solution is smooth and independent of time. In the absence of friction, the first momentum equation for smooth steady state flows becomes

$$\partial_\ell(\alpha\rho u^2) + \alpha\partial_\ell p = -g\alpha\rho\sin(\theta).$$

Furthermore, $Q = \alpha\rho u$, $Q_s = \alpha_s\rho_s u_s$ are constant by conservation of mass. The above equation can be re-written as

$$\partial_\ell\left(\frac{u^2}{2}\right) + \frac{1}{\rho}\partial_\ell p = -g\sin\theta.$$

Using the relations (2.4), (2.5) and (2.6), one obtains

$$\frac{1}{\rho}\frac{\partial p}{\partial\ell} = \frac{c^2}{\rho}\partial_\ell\rho = \eta\gamma\rho^{\gamma-2}\partial_\ell\rho = \eta\gamma\partial_\ell\left(\frac{\rho^{\gamma-1}}{\gamma-1}\right) = \partial_\ell\left(\frac{c^2}{\gamma-1}\right),$$

which implies that $h+G$ is constant for any of the cases in this proposition.

Regarding the solid phase, one also has $\rho_s^{-1}\partial_\ell p_s = \partial_\ell(c_s^2/(\gamma_s-1))$. However, the momentum equation in the solid phase becomes

$$\partial_\ell\left(\frac{u_s^2}{2}\right) + \frac{1}{\rho_s}\partial_\ell p_s = \frac{p-p_s}{\alpha_s\rho_s}\partial_\ell\alpha_s - g\sin\theta.$$

If α_s is constant, then h_s+G is invariant as stated in case (i). On the other hand, if u_s vanishes (as in solid sedimentation), then equation (2.7) is satisfied.

□

Note: equation (2.7) can be re-written as

$$\partial_\ell\left(\alpha\rho u^2 + \alpha p + \alpha_s p_s\right) = -g(\alpha\rho + \alpha_s\rho_s)\sin\theta$$

for steady states of type (ii). As a result, smooth steady-state flows in horizontal pipes have the gas enthalpy and $\alpha\rho u^2 + \alpha p + \alpha_s p_s$ as two invariants. Furthermore, Proposition 2.2 can be generalized to any barotropic pressure if $c^2/(\gamma-1)$ is replaced by $\int p'(\rho)/\rho\, d\rho$.

Equation (2.7) can be replaced by the sum of the two momentum fluxes as another invariants when $\theta = 0$. In vertical or deviated pipes, the enthalpy must be in balance with the vertically integrated gravity acceleration. In the first type of steady states, the gas- and solid- subsystems decouple and reduce to the standard isentropic Euler equations. On the other hand, for a non-uniform solid volume fraction one requires the solid velocity to vanish giving the second type of steady states. We note that this type of steady states involves four conditions (including $u_s = 0$ and the equation for the solid pressure) but five variables. That implies that one can obtain a much larger class of steady states compared to the one phase Euler model. Namely, if we fix α_s, the gas phase invariants Q and $h+G$ determine the gas phase variables when appropriate boundary conditions are imposed. Then the solid density (or equivalently the solid pressure) is determined by equation (2.7). Each solid volume fraction profile gives us a corresponding equilibrium state for the above invariants. One of the implications is that if a perturbation is imposed on top of a steady state, such perturbation propagates and eventually leaves the domain. As a result, the long time behavior of the solution is another steady state. However, the final steady state may differ from the initial one. A similar observation is done in Hernandez-Duenas [18] for shallow water flows with horizontal density gradients, which does not replicate in regular shallow water systems.

3. The semi-discrete central-upwind scheme

The semi-discrete central-upwind scheme is designed in general for hyperbolic systems of balance laws [23]. We write system (2.1) in the general form as

$$\mathbf{W}_t + \partial_\ell\mathbf{F}(\mathbf{W}) = \mathbf{S}(\mathbf{W},\ell), \tag{3.1}$$

where

$$\mathbf{W} = \begin{pmatrix} \alpha\rho \\ \alpha\rho u \\ \alpha_s\rho_s \\ \alpha_s\rho_s u_s \\ \rho_s \end{pmatrix}, \quad \mathbf{F}(\mathbf{W}) = \begin{pmatrix} \alpha_g\rho_g u_g \\ \alpha_g(\rho_g u_g^2 + p_g) \\ \alpha_s\rho_s u_s \\ \alpha_s(\rho_s u_s^2 + p_s) \\ \rho_s u_s \end{pmatrix} \tag{3.2}$$

and

$$\mathbf{S} = \begin{pmatrix} 0 \\ -p\partial_\ell\alpha_s - g\alpha\rho\sin(\theta(\ell)) + F_{dg} \\ 0 \\ p\partial_\ell\alpha_s - g\alpha_s\rho_s\sin(\theta(\ell)) - F_{dg} \\ 0 \end{pmatrix} \tag{3.3}$$

are the vectors of conserved variables, flux and non-conservative products respectively.

We partition the spatial domain into the grid cells $I_j := [\ell_{j-\frac{1}{2}}, \ell_{j+\frac{1}{2}}]$, where $\Delta\ell$ is the cell's length, $\ell_{j\pm\frac{1}{2}} = \ell_j \pm \frac{\Delta\ell}{2}$ and ℓ_j is the center of the grid cell I_j. Let us denote by $\overline{\overline{\mathbf{W}}}_j$ the computed cell average of the exact solution $\mathbf{W}(\ell,t)$ over the cell I_j,

$$\overline{\overline{\mathbf{W}}}(t) = \frac{1}{\Delta\ell}\int_{\ell_{j-\frac{1}{2}}}^{\ell_{j+\frac{1}{2}}} \mathbf{W}(\ell,t)\,\mathrm{d}\ell. \tag{3.4}$$

When integrating Equation (3.1) over each cell I_j, we obtain the semidiscrete formulation

$$\frac{\mathrm{d}}{\mathrm{d}t}\overline{\overline{\mathbf{W}}}_j(t) + \frac{1}{\Delta\ell}\Big(\mathbf{F}(\mathbf{W}(\ell_{j+\frac{1}{2}},t)) - \mathbf{F}(\mathbf{W}(\ell_{j-\frac{1}{2}},t))\Big) = \frac{1}{\Delta\ell}\int_{\ell_{j-\frac{1}{2}}}^{\ell_{j+\frac{1}{2}}} \mathbf{S}(\mathbf{W}(\ell,t),\ell)\ \mathrm{d}\ell, \tag{3.5}$$

On the other hand, we will denote by $\overline{\mathbf{W}}$ the numerical approximation of $\overline{\overline{\mathbf{W}}}$. For the sake of simplicity, we will often refer to $\overline{\mathbf{W}}$ as the cell average. Equation (3.5) is then approximated by

$$\frac{\mathrm{d}}{\mathrm{d}t}\overline{\mathbf{W}}_j(t) = -\frac{\mathbf{H}_{j+\frac{1}{2}} - \mathbf{H}_{j-\frac{1}{2}}}{\Delta\ell} + \overline{\mathbf{S}}_j. \tag{3.6}$$

Here $\overline{\mathbf{S}}_j$ is a discretization of the non-conservative products and source terms to be described below. The flux at the cell interfaces, *i.e.*, $\mathbf{F}(\mathbf{W}(\ell_{j\pm\frac{1}{2}}),t)$, is approximated by the numerical flux $\mathbf{H}_{j\pm\frac{1}{2}}(t)$ given by Kurganov and Tadmor [23]

$$\mathbf{H}_{j\pm\frac{1}{2}}(t) = \frac{a^+_{j\pm\frac{1}{2}}\mathbf{F}\left(\mathbf{W}^-_{j\pm\frac{1}{2}}(t)\right) - a^-_{j\pm\frac{1}{2}}\mathbf{F}\left(\mathbf{W}^+_{j\pm\frac{1}{2}}(t)\right)}{a^+_{j\pm\frac{1}{2}} - a^-_{j\pm\frac{1}{2}}} + \frac{a^+_{j\pm\frac{1}{2}}a^-_{j\pm\frac{1}{2}}}{a^+_{j\pm\frac{1}{2}} - a^-_{j\pm\frac{1}{2}}}\left(\mathbf{W}^+_{j\pm\frac{1}{2}}(t) - \mathbf{W}^-_{j\pm\frac{1}{2}}(t)\right), \tag{3.7}$$

where $\mathbf{W}^\pm_{j\pm\frac{1}{2}}(t)$ is a non-oscillatory piecewise polynomial reconstruction of the cell averages. The one-sided local speeds in this scheme are approximated using the eigenvalues of the Jacobian:

$$a^-_{j\pm\frac{1}{2}} = \min\left\{u^+_{j\pm\frac{1}{2}} - c^+_{j\pm\frac{1}{2}}, u^+_{s,j\pm\frac{1}{2}} - c^+_{s,j\pm\frac{1}{2}}, 0\right\}, \quad a^+_{j\pm\frac{1}{2}} = \max\left\{u^+_{j\pm\frac{1}{2}} + c^+_{j\pm\frac{1}{2}}, u^+_{sj\pm\frac{1}{2}} + c^+_{s,j\pm\frac{1}{2}}, 0\right\}. \tag{3.8}$$

We note that $a^+_{j\pm\frac{1}{2}} - a^-_{j\pm\frac{1}{2}} > 0$ unless $\rho^\pm_{j\pm\frac{1}{2}}$, $\rho^\pm_{s,j\pm\frac{1}{2}}$ and $u^\pm_{j\pm\frac{1}{2}}$, $u^\pm_{s,j\pm\frac{1}{2}}$ all vanish in a collapsed state with vanishing velocity. However, we always start with positive (although possibly small) density values.

For any quantity $v(\ell,t)$, the interface point-values $v_{j\pm\frac{1}{2}}(t)$ are recovered from the approximated cell averages $\bar{v}_j(t)$ via a piecewise linear reconstruction

$$v(\ell,t) = \bar{v}_j(t) + v'_j(t)(\ell - \ell_j), \tag{3.9}$$

where v'_j are limited slopes calculated as [45],

$$v'_j(t) = \frac{1}{\varDelta\ell}\operatorname{minmod}(\alpha_m\varDelta_-\overline{v_j}(t),\ \varDelta_0\overline{v_j}(t),\ \alpha_m\varDelta_+\overline{v_j}(t)). \tag{3.10}$$

This reconstruction satisfies the following essential properties: conservation of cell averages, second order accuracy in smooth regions, a non-oscillatory behavior and preservation of positivity in α, ρ, α_s and ρ_s. Here $1 \le \alpha_m < 2$ and

$$\operatorname{minmod}(x_1, x_2, x_3, \ldots, x_k) = \begin{cases} \min_j(x_j) & \text{if } \ x_j > 0\ \forall j, \\ \max_j(x_j) & \text{if } \ x_j < 0\ \forall j, \\ 0 & \phantom{\text{if }}\ \text{otherwise.} \end{cases}$$

Unless otherwise noted, we set $\alpha_m = 1.5$ for this minmod parameter. Different values of α_m provide different limited slopes. However, all of them are second order reconstruction in smooth regions and the numerical approximations are not sensitive to a particular choice of α_m. See Kurganov and Tadmor [23] for more details.

The non-conservative products in the momentum equations are approximated by

$$\overline{\overline{p\partial_\ell\alpha_s}} = \frac{1}{\varDelta\ell}\int_{x_{j-\frac{1}{2}}}^{x_{j+\frac{1}{2}}} p\frac{\partial\alpha_s(\ell,t)}{\partial\ell}\mathrm{d}\ell \approx \bar{p}_j\frac{\alpha^-_{s,j+\frac{1}{2}}(t) - \alpha^+_{s,j-\frac{1}{2}}(t)}{\varDelta\ell}. \tag{3.11}$$

The other source terms are approximated with their cell averages only, so that $\bar{F}_{dg,j} = -\frac{3}{4}\frac{C_d}{d_p}\bar{\alpha}_{s,j}|\bar{u}_j - \bar{u}_{s,j}|(\bar{u}_j - \bar{u}_{s,j})$, and

$$\bar{\mathbf{S}}_j = \begin{pmatrix} 0 \\ -\bar{p}_j\dfrac{\alpha^-_{s,j+\frac{1}{2}}(t) - \alpha^+_{s,j-\frac{1}{2}}(t)}{\varDelta\ell} - g\bar{\alpha}_j\bar{\rho}_j\sin(\theta(\ell_j)) + \bar{F}_{dg,j} \\ 0 \\ \bar{p}_j\dfrac{\alpha^-_{s,j+\frac{1}{2}}(t) - \alpha^+_{s,j-\frac{1}{2}}(t)}{\varDelta\ell} - g\bar{\alpha}_{s,j}\bar{\rho}_{s,j}\sin(\theta(\ell_j)) - \bar{F}_{dg,j} \\ 0 \end{pmatrix}. \tag{3.12}$$

The above discretization is chosen to satisfy the well-balanced property (see Appendix A). There can be other discretizations of this term satisfying second order accuracy in smooth regions and satisfying the well-balanced property but we do not expect significant differences in the numerical results. Path-conservative schemes in Parés [32] show some considerations one can take when choosing discretizations in the presence of non-conservative products.

3.1. A positivity preserving reconstruction

For the positivity preserving property, we follow [21]. The first step is a reconstruction that preserves the positivity of the desired variables. The details are given in the following proposition.

Proposition 3.1. *Given a positive quantity $\bar{A}_j \ge 0$ such as $\alpha\rho$, $\alpha_s\rho_s$, α and α_s, the reconstructed interface values $A^{\pm}_{j\pm\frac{1}{2}}$ given by* (3.9) *and* (3.10) *are also positive.*

Proof. For a given cell I_j, the reconstruction depends on the values $\bar{A}_{j-1}$, $\bar{A}_j$ and $\bar{A}_{j+1}$. One can determine four possibilities, two of them illustrated in Figure 2. In the first case the set $\{A_{j-1},\ A_j,\ A_{j+1}\}$ represents a local minimum so that $\varDelta_+\overline{\mathbf{W}}_j$ and $\varDelta_-\overline{\mathbf{W}}_j$ have opposite signs, such as in Figure 2b. The reconstruction in those cases is trivial. The local maximum case is analogous. In the case where the average values are increasing $\bar{A}_{j-1} \leq \bar{A}_j \leq \bar{A}_{j+1}$, and for any $\alpha_m \in (1,2)$ we have

$$0 \leq A_j' = \operatorname{minmod}\left(\alpha_m \frac{A_{j+1}-A_j}{\Delta\ell},\ \frac{A_{j+1}-A_{j-1}}{2\Delta\ell},\ \alpha_m \frac{A_j - A_{j-1}}{\Delta\ell}\right) \leq \frac{2(A_j - A_{j-1})}{\Delta\ell},$$

so that

$$A^-_{j+\frac{1}{2}} = \bar{A}_j + \frac{\Delta\ell}{2} A_j' \geq \bar{A}_j > 0,\ A^+_{j-\frac{1}{2}} = \bar{A}_j - \frac{\Delta\ell}{2} A_j' \geq A_{j-1} > 0.$$

The decreasing case $\bar{A}_{j-1} \geq \bar{A}_j \geq \bar{A}_{j+1}$ is analogous. ☐

3.2. Time evolution

Once the interface values, the numerical fluxes and the average of the source term have been calculated, the ODE system (3.6) is integrated in time using the second order Strong Stability Preserving Runge-Kutta scheme [17],

$$\mathbf{W}^{(1)} = \mathbf{W}^{(0)} + \Delta t\, \mathbf{C}[\mathbf{W}^{(0)}], \tag{3.13a}$$

$$\mathbf{W}^{(2)} = \frac{1}{2}\mathbf{W}^{(0)} + \frac{1}{2}\left(\mathbf{W}^{(1)} + \Delta t\, \mathbf{C}[\mathbf{W}^{(1)}]\right), \tag{3.13b}$$

$$\overline{\mathbf{W}}(t+\Delta t) := \mathbf{W}^{(2)}, \tag{3.13c}$$

with the Runge-Kutta fluxes

$$\mathbf{C}[\mathbf{W}(t)] = -\frac{\mathbf{H}_{j+\frac{1}{2}}(v(t)) - \mathbf{H}_{j-\frac{1}{2}}(v(t))}{\Delta\ell} + \overline{\mathbf{S}}_j(t), \tag{3.14}$$

and $\overline{\mathbf{S}}_j(t)$ calculated according to (3.11). The time step Δt is determined so as to satisfy the CFL restriction

$$\begin{aligned}\frac{\Delta t}{\Delta\ell} \max_{j=1:N} \Bigg\{ & \frac{a^+_{j+\frac{1}{2}}(\alpha\rho)^-_{j+\frac{1}{2}} - a^-_{j-\frac{1}{2}}(\alpha\rho)^+_{j-\frac{1}{2}}}{2\overline{(\alpha\rho)}_j},\ \frac{a^+_{j+\frac{1}{2}}(\alpha_s\rho_s)^-_{j+\frac{1}{2}} - a^-_{j-\frac{1}{2}}(\alpha_s\rho_s)^+_{j-\frac{1}{2}}}{2\overline{(\alpha_s\rho_s)}_j},\\ & \frac{a^+_{j+\frac{1}{2}}(\alpha\rho_s)^-_{j+\frac{1}{2}} - a^-_{j-\frac{1}{2}}(\alpha\rho_s)^+_{j-\frac{1}{2}}}{2\overline{(\alpha\rho_s)}_j},\ \frac{a^+_{j+\frac{1}{2}}(\rho_s)^-_{j+\frac{1}{2}} - a^-_{j-\frac{1}{2}}(\rho_s)^+_{j-\frac{1}{2}}}{2\overline{(\alpha\rho)}_j} \Bigg\} \leq \frac{1}{2}.\end{aligned} \tag{3.15}$$

For the ease of notation we have denoted again by bars, $\overline{\mathbf{W}}(t+\Delta t)$, the numerical solution at the next time step, which is approximated by the Runge-Kutta time integration (3.13).

The following proposition shows that this CFL condition guarantees the positivity of the quantities α, ρ, α_s and ρ_s when the solution is evolved according to the Runge-Kutta time integration (3.13). Since $\alpha + \alpha_s = 1$, the positivity of α and α_s is equivalent to the inequality $0 \leq \alpha_s \leq 1$, which is particularly tricky.

Proposition 3.2. *Consider the scheme given by equations* (3.13) *and* (3.14) *with numerical flux as in* (3.7), *source term discretization given by* (3.12) *and CFL restriction as in* (3.15). *If the cell averages* $\bar{\rho}_j(t)$, $\bar{\rho}_{s,j}$, $\bar{\alpha}_{s,j}$ *are positive and* $0 \leq \alpha_{s,j} \leq 1$ *for every* j, *then the time evolution preserves positivity and respects the same inequalities*

$$\bar{\rho}_j(t+\Delta t) \geq 0, \quad \bar{\rho}_{s,j}(t+\Delta t) \geq 0 \quad \text{and} \quad 0 \leq \bar{\alpha}_{s,j}(t+\Delta t) \leq 1 \ \ \forall j.$$

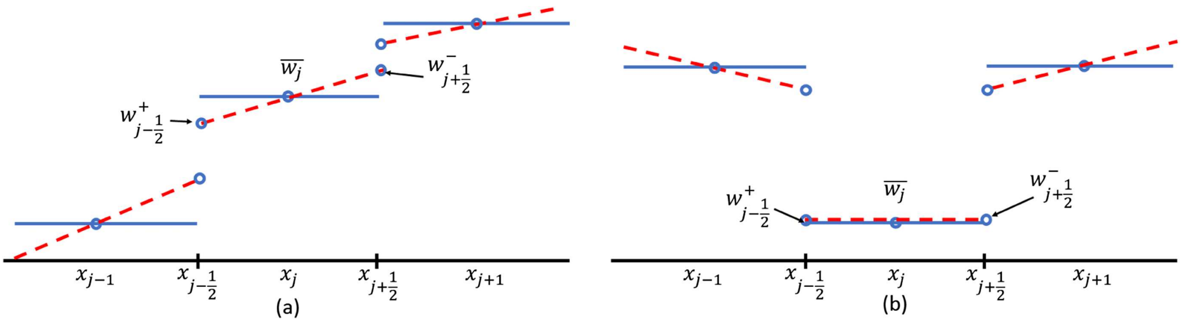

FIGURE 2. Linear reconstruction of the cell averages. The circles represent the interface values using a linear reconstruction (3.9) and (3.10) (dashed line) recovered from the cell averages (horizontal solid line). The left panel shows a case where the cell averaged data is monotone while the right panel describes a case with a local minimum.

Proof. Since the Runge-Kutta scheme (3.13) is a convex combination of forward Euler steps, it is sufficient to show the property for just one Euler step. We apply the following inequalities to any of the quantities $A = \alpha\rho$ or $A_s \in \{\alpha_s\rho_s,\ \rho_s,\ \alpha\rho_s = \rho_s - \alpha_s\rho_s\}$. All of these quantities satisfy advection equations of the form

$$\partial_t A + \partial_\ell(Au) = 0, \quad \partial_t A_s + \partial_\ell(A_s u_s) = 0.$$

Let $Q = Au$ and $Q_s = A_s u_s$ be the fluxes of the corresponding conserved variables. The proof for the gas or the solid phase is analogous, so we do it only for A. We note that

$$\begin{aligned}
\bar{A}_j(t+\Delta t) &= \bar{A}_j - \frac{\Delta t}{\Delta \ell}\left[\frac{a^+_{j+\frac12}Q^-_{j+\frac12} - a^-_{j+\frac12}Q^+_{j+\frac12}}{a^+_{j+\frac12}-a^-_{j+\frac12}} - \frac{a^+_{j-\frac12}Q^-_{j-\frac12} - a^-_{j-\frac12}Q^+_{j-\frac12}}{a^+_{j-\frac12}-a^-_{j-\frac12}}\right] \\
&\quad - \frac{\Delta t}{\Delta\ell}\frac{a^+_{j+\frac12}a^-_{j+\frac12}}{a^+_{j+\frac12}-a^-_{j+\frac12}}\left(A^+_{j+\frac12}-A^-_{j+\frac12}\right) + \frac{\Delta t}{\Delta\ell}\frac{a^+_{j-\frac12}a^-_{j-\frac12}}{a^+_{j-\frac12}-a^-_{j-\frac12}}\left(A^+_{j-\frac12}-A^-_{j-\frac12}\right) \\
&= \bar{A}_j - \frac{\Delta t}{\Delta\ell}a^+_{j+\frac12}\frac{u^-_{j+\frac12}-a^-_{j+\frac12}}{a^+_{j+\frac12}-a^-_{j+\frac12}}A^+_{j+\frac12} + \frac{\Delta t}{\Delta\ell}a^-_{j-\frac12}\frac{a^+_{j-\frac12}-u^+_{j-\frac12}}{a^+_{j-\frac12}-a^-_{j-\frac12}}A^+_{j-\frac12} \\
&\quad - \frac{\Delta t}{\Delta\ell}a^-_{j+\frac12}\frac{a^+_{j+\frac12}-u^+_{j+\frac12}}{a^+_{j+\frac12}-a^-_{j+\frac12}}A^+_{j+\frac12} + \frac{\Delta t}{\Delta\ell}a^+_{j-\frac12}\frac{u^-_{j-\frac12}-a^-_{j-\frac12}}{a^+_{j-\frac12}-a^-_{j-\frac12}}A^-_{j-\frac12} \\
&\geq \bar{A}_j - \frac{\Delta t}{\Delta\ell}a^+_{j+\frac12}\frac{u^-_{j+\frac12}-a^-_{j+\frac12}}{a^+_{j+\frac12}-a^-_{j+\frac12}}A^+_{j+\frac12} + \frac{\Delta t}{\Delta\ell}a^-_{j-\frac12}\frac{a^+_{j-\frac12}-u^+_{j-\frac12}}{a^+_{j-\frac12}-a^-_{j-\frac12}}A^+_{j-\frac12}
\end{aligned} \tag{3.16}$$

since $a^+_{j+\frac12} \geq u^+_{j+\frac12}$ and $a^-_{j-\frac12} \leq u^-_{j-\frac12}$ by equation (3.8). On the other hand, we also have

$$\frac{u^-_{j+\frac12}-a^-_{j+\frac12}}{a^+_{j+\frac12}-a^-_{j+\frac12}} \leq 1, \quad \frac{a^+_{j-\frac12}-u^+_{j-\frac12}}{a^+_{j-\frac12}-a^-_{j-\frac12}} \leq 1,$$

which implies

$$\bar{A}_j(t+\Delta t) \geq \bar{A}_j - \frac{\Delta t}{\Delta\ell}a^+_{j+\frac12}A^-_{j+\frac12} + \frac{\Delta t}{\Delta\ell}a^-_{j-\frac12}A^+_{j-\frac12}.$$

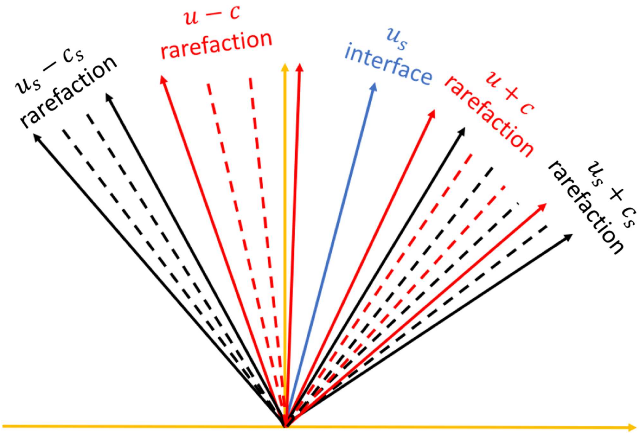

FIGURE 3. Solution's configuration for the Riemann problem in (4.1) and (4.2).

We apply the above inequalities to the quantities $A = \alpha\rho$, $\alpha_s\rho_s$ and ρ_s. The CFL condition (3.15) guarantees the positivity of ρ_s, α_s and $\alpha\rho$. We still need to show the positivity of α and therefore of ρ. We note that subtracting the fifth line from the third in Equation (2.1) we get

$$(\alpha\rho_s)_t + \partial_\ell(\alpha\rho_s u_s) = 0.$$

So, the time restriction

$$\frac{\Delta t}{\Delta \ell}\frac{a^+_{j+\frac{1}{2}}(\alpha\rho_s)^-_{j+\frac{1}{2}} - a^-_{j-\frac{1}{2}}(\alpha\rho_s)^+_{j-\frac{1}{2}}}{2\overline{(\alpha\rho_s)}_j} \le \frac{1}{2}$$

also guarantees the positivity of α, which together with the positivity of α_s gives us $0 \le \alpha_s(t+\Delta t) \le 1$. □

4. NUMERICAL EXAMPLES

In this section we present a set of numerical tests to show the merits of the scheme. In addition, we use the model to numerically study accumulation of solids in deviated pipes and qualitatively compare our observations with results obtained in the literature using other approaches.

4.1. A Riemann problem

As it was mentioned above, weak solutions based on the theory of non-conservative products in Dal Maso *et al.* [10] allows us to construct solutions to the Riemann problem for two-phase flows. Even though system (2.1) is not in conservation form, each wave field is either GNL or LD and it can help in the existence of weak solutions and uniqueness of jump conditions.

For the first numerical example, we consider a Riemann problem where the initial condition is piecewise constant with a jump discontinuity in the middle of the domain. The Riemann solution can have either shock or rarefaction waves in two of the wave families in each phase plus the interface that connects both phases through porosity jumps. In particular, the solution to the problem below consists of the following configuration. Both phases have a rarefaction wave to each side of the interface. The gas and solid rarefaction waves to the right of the interface overlap. See Figure 3 for a schematic representation of this configuration.

The arclength domain here is $[0\,\text{km}, 2\,\text{km}]$, the constant entropies are $\eta = 2.32\times10^{-1}$ Pa, $\eta_s = 1.54\times10^{-4}$ Pa and the polytropic exponents are $\gamma = 1.4$, $\gamma_s = 2.05$ respectively. The stiffening pressure here is $p_o = 848.76$ Pa. Here we consider a horizontal pipe ($\theta = 0$) with no interfacial friction ($F_{dg} = 0$). Since the pipe is horizontal, the arclength coincides with the horizontal coordinate ($\ell = x$).

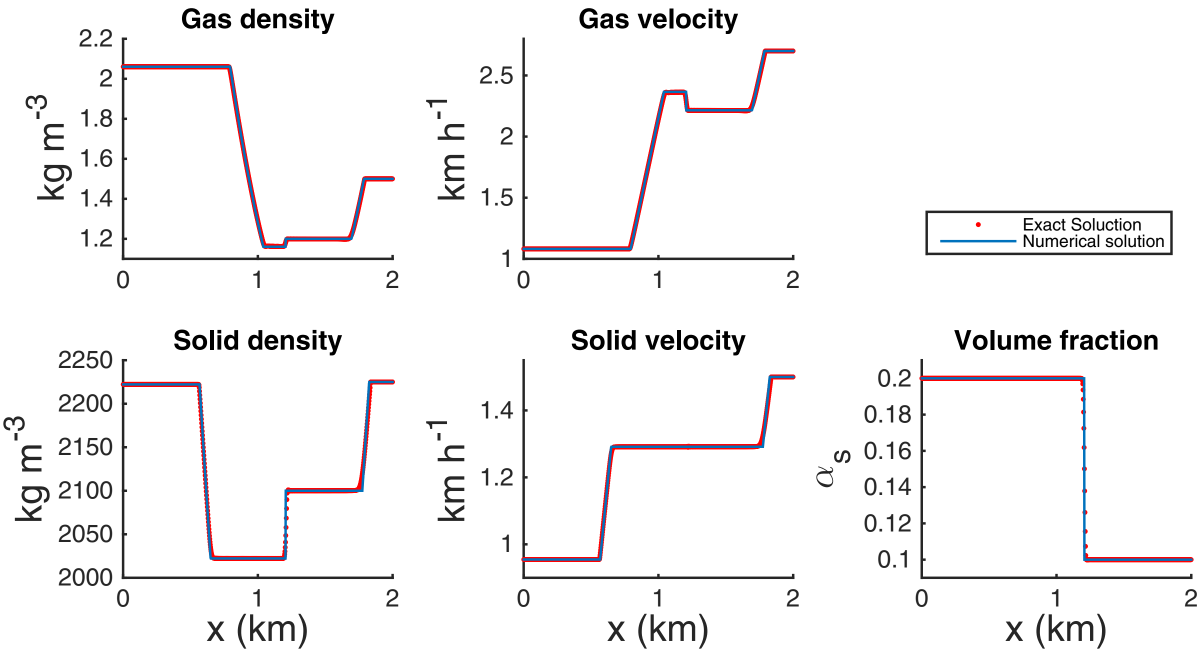

FIGURE 4. Exact (solid blue) and numerical (solid red) solutions are exhibited at time $T = 0.16$. *Top*: the gas density (*left*) and velocity (*middle*). *Bottom*: Solid density (*left*), solid velocity (*middle*) and solid volume fraction (*right*). The initial conditions are (4.1) and (4.2) and the resolution is $\Delta\ell = 2\,\mathrm{m}$ (1000 gridpoints).

The initial conditions are given by

$$(\rho, u)(\ell, 0) = \begin{cases} \left(2.06\,\mathrm{kg\,m^{-3}},\ 1.08\,\mathrm{km\,h^{-1}}\right) & \text{if } \ 0\,\mathrm{km} \le \ell < 1\,\mathrm{km}, \\ \left(1.5\,\mathrm{kg\,m^{-3}},\ 2.7\,\mathrm{km\,h^{-1}}\right) & \text{if } \ 1\,\mathrm{km} \le \ell \le 2\,\mathrm{km}, \end{cases} \tag{4.1}$$

and

$$(\rho_s, u_s, \alpha_s)(\ell, 0) = \begin{cases} (2222.2\,\mathrm{kg\,m^{-3}},\ 9.54 \times 10^{-1}\,\mathrm{km\,h^{-1}},\ 2 \times 10^{-1}) & \text{if } \ 0\,\mathrm{km} \le \ell < 1\,\mathrm{km}, \\ (2225\,\mathrm{kg\,m^{-3}},\ 1.5\,\mathrm{km\,h^{-1}},\ 1 \times 10^{-1}) & \text{if } \ 1\,\mathrm{km} \le \ell \le 2\,\mathrm{km}, \end{cases} \tag{4.2}$$

for the gas and solid phases respectively. The solution to this Riemann problem consists of a left solid rarefaction wave followed by left gas rarefaction wave, a compaction wave, a gas right rarefaction wave with a right solid rarefaction wave inside. See the schematic in Figure 3. The exact solution is obtained using the algorithm in Appendix B. The intermediate states are

$$\rho_{m,L} = 1.16\,\mathrm{kg\,m^{-3}},\ u_{m,L} = 2.37\,\mathrm{km\,h^{-1}},\ \rho_{m,R} = 1.2\,\mathrm{kg\,m^{-3}},\ u_{m,R} = 2.21\,\mathrm{km\,h^{-1}},$$

$$\rho_{s,m,L} = 2022.2\,\mathrm{kg\,m^{-3}},\ u_{s,m,L} = 1.29\,\mathrm{km\,h^{-1}},\ \rho_{s,m,R} = 2100\,\mathrm{kg\,m^{-3}},\ u_{s,m,R} = 1.29\,\mathrm{km\,h^{-1}}.$$

Figure 4 displays the exact solution (blue solid line) and compares it with the numerical approximation (red solid line) at time $T = 3$ min, using free boundary conditions. The top row shows the gas density (*left*) and velocity (*middle*), while the bottom row shows the solid density (*left*), solid velocity (*middle*) and solid volume fraction (*right*) as a function of arclength ℓ. We note that the solid volume fraction is a non-dimensional quantity between 0 and 1 and it represents the fraction of the solid phase in the duct. The resolution is $\Delta\ell = 2\,\mathrm{m}$ (1000

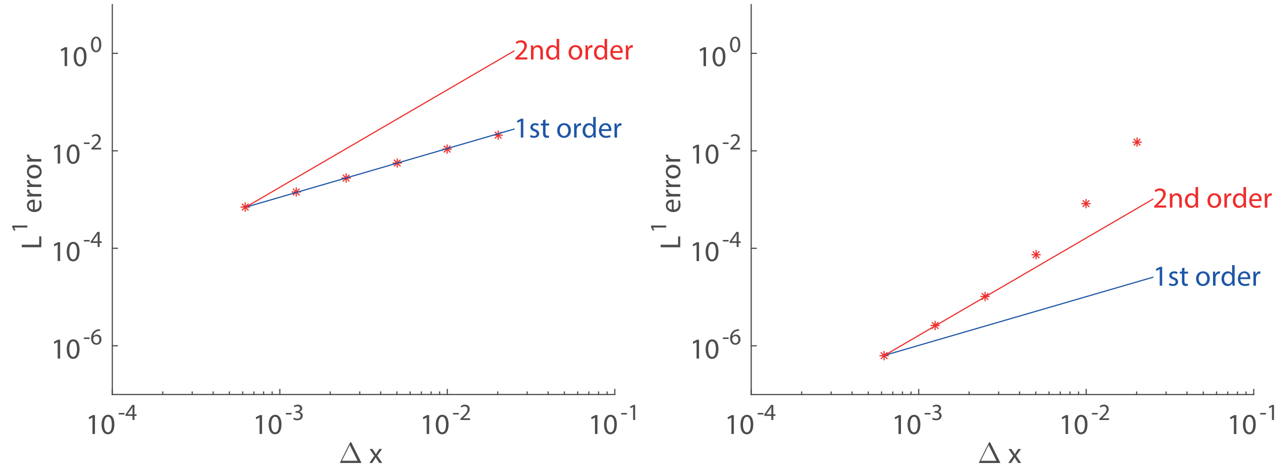

FIGURE 5. *Left panel*: log–log plot of the relative error $E = E_\rho + E\rho_s + E_u + E_{u_s} + E_{\alpha_s}$ *versus* Δx for a solution consisting of two rarefaction waves in each phase and a compaction wave. Also shown are a red line with slope 2 and a blue line with slope 1, representing second and first order of accuracy, respectively. *Right panel*: relative error measured inside the gas rarefaction in the range $x \in [0.85, 0.95]$.

gridpoints). We point out that the numerical and exact solutions are in good agreement. The compaction wave visible in the solid volume fraction is traveling to the right. The numerical solution is also very precise near that wave. For instance, the solid velocity is flat near the compaction wave and the numerical solution captures that Riemann invariant accurately. Other Riemann problems with a more pronounced jump in the density across the compaction wave might introduce larger errors. This can be alleviated with a hybrid strategy as in [18, 19]. However, our interest in the following numerical tests use volume fractions with relatively small jumps.

We note that the initial solid density was chosen much higher than that of the gas phase. See for example the numerical tests in García-Cascales *et al.* [14]. The solid phase corresponds to a compressible granular flow and the solid density is expected to vary weakly. In the present simulation the solid density varies from 2000 $\mathrm{kg\,m^{-3}}$ to 2225 $\mathrm{kg\,m^{-3}}$, which represents about 5.6% of its maximum value.

The relative error of a quantity q in the domain $[0, L]$ is defined as

$$E_q(t) := \frac{1}{L}\int_0^L \frac{|q(x,t) - q_{\text{exact}}(x,t)|}{|q_{\text{exact}(x,t)}|}\mathrm{d}x.$$

The availability of exact solutions to the Riemann problem can help us study the accuracy of the numerical scheme. Godunov's theorem states that monotone linear numerical schemes are at most first order accurate ([27], Thm. 15.5). The central-upwind scheme is by construction second order accurate in smooth regions and first order accurate near discontinuities. See for instance [20] where the convergence rate is analyzed only when the solution is smooth. The left panel in Figure 5 shows a graph of the relative error $E = E_\rho + E\rho_s + E_u + E_{u_s} + E_{\alpha_s}$ as a function of Δx in a log–log plot. Also shown are a red line with slope 2 and a blue line with slope 1 which represent second and first order of accuracy. The convergence rate is about 1.0027 for the total L^1 relative error E. For some variables like u_s, the convergence rate was slightly higher (1.34). This can be explained by the fact that the solution in Figure 4 has a discontinuity near the compaction wave, which affects the convergence rate. However, second order accuracy can be observed if we measure the relative error only near the rarefaction wave in the range $x \in [0.85, 0.95]$. For that purpose, we take as initial conditions the exact solution at $t = 0.08$ and stop at $t = 0.16$ to avoid the approximation near the discontinuity to contaminate the rest of the solution. This computation is shown in the right panel of Figure 5, showing a convergence rate of about 2.0033.

The numerical tests in the following sections incorporate gravity in a vertically deviated pipe. A moderate solid density will be considered for those cases so that the gas pressure and discharge at the bottom of the pipe can push the solid particles upward. One of the goals here is the analysis of the dynamics where a solid accumulation in certain regions of the pipes can be observed. As a result, we are assuming the solid phase consists of sand with relatively low solid density. In a future work, we will include a liquid phase (muds) to further investigate this phenomenon.

4.2. Convergence to a steady state

As we observed in Proposition 2.2, there are two types of steady states. In one of them, the solid volume fraction is constant, the two phases decompose and have no interactions, and the steady states in each phase are characterized by two invariants. The other type of steady states arises when the solid velocity vanishes. It can be interpreted as sedimentation of the solid phase. The gas phase is characterized by two invariants, and the solid density satisfies equation (2.7). This leaves one variable free: the solid volume fraction. As a result, one can have infinitely many steady states associated to the same invariants, one for each solid volume fraction profile. This situation has also been reported in a different context. In Hernandez-Duenas [18], steady states arbitrarily close to each other also appear in shallow water flows with horizontal density gradients.

Under appropriate boundary conditions, the solution is expected to equilibrate as $t \to \infty$, reaching a steady state. The pipe is described by arclength ℓ in the domain $[0\,\mathrm{km}, 5\,\mathrm{km}]$ and the angle with respect to the horizontal line is given by

$$\theta(\ell) = 0.99\frac{\pi}{2}\frac{\ell}{5\,\mathrm{km}}\cdot$$

That is, the angle is increasing linearly with respect to arclength. The pipe is horizontal at the bottom and almost vertical at the surface. The gravitational constant is $g = 9.81\,\mathrm{m\,s^{-2}}$, $\gamma = 1.4$, $\gamma_s = 1.92$, $\eta = 2 \times 10^4$ Pa, $\eta_s = 3.14 \times 10^3$ Pa and $F_{dg} = 0$. The entropy values here are those that will be used in Section 4.4. The stiffening pressure here is $p_o = 848.76$ Pa. The initial conditions are

$$(\rho,\ u,\ \rho_s,\ u_s,\ \alpha_s)(\ell, 0) = \left(10\,\mathrm{kg\,m^{-3}},\ 0\,\mathrm{km\,h^{-1}},\ 20\,\mathrm{kg\,m^{-3}},\ 0\,\mathrm{km\,h^{-1}}, 0.7 - \frac{0.4\ell}{5\,\mathrm{km}}\right)\cdot \tag{4.3}$$

At the left boundary (bottom), we extrapolate all the variables at out flow ($u + c < 0$ or $u_s + c_s < 0$) and impose $\rho_{\mathrm{in}} = 10\,\mathrm{kg\,m^{-3}}$, $u_{\mathrm{in}} = 10\,\mathrm{km\,h^{-1}}$, $\rho_{s,\mathrm{in}} = 20\,\mathrm{kg\,m^{-3}}$, $u_{s,\mathrm{in}} = 0\,\mathrm{km\,h^{-1}}$ and $\alpha_{s,\mathrm{in}} = 0.7$ at inflow. At the right boundary (surface), we extrapolate all the variables at out flow ($u + c > 0$ or $u_s + c_s > 0$) and impose $\rho_{\mathrm{out}} = 6.14\,\mathrm{kg\,m^{-3}}$, $u_{\mathrm{out}} = 6.95\,\mathrm{km\,h^{-1}}$, $\rho_{s,\mathrm{out}} = 18.67\,\mathrm{kg\,m^{-3}}$, $u_{s,\mathrm{in}} = 0\,\mathrm{km\,h^{-1}}$ and $\alpha_{s,\mathrm{out}} = 0.3$ at inflow.

Figure 6 shows the numerical (red dotted line) and exact (blue solid line) solutions for the problem with the above initial conditions at time $T = 30$ min and resolution $\Delta\ell = 10$ m (500 gridpoints). The top row shows the gas density (*left*), gas velocity (*middle*) and solid volume fraction (*right*). The bottom row shows the solid density (*left*), solid velocity (*middle*) and an illustration of the pipe (*right*). Such illustration shows the pipe in the $x{-}z$ plane and a red solid curve places the solid phase below it. The model does not involve a given cross-section thickness and this illustration only shows a proportion of the area occupied by each phase according to the volume fraction. We note that the exact solution is computed by solving the equations in Proposition 2.2 for the solid volume fraction given by the numerical solution at the final time as in Figure 6.

4.3. A vacuum problem

In Perthame and Simeoni [33] the authors construct a kinetic scheme to compute the numerical solution of the Saint-Venant equations commonly used to describe physical situations such as flows in rivers or coastal areas. As it is observed in Perthame and Simeoni [33] the main problem of several methods for solving hyperbolic systems of conservation laws with source terms is related to the approximation of a source term to ensure the numerical preservation of properties fulfilled by the continuous model. Several numerical methods fail to satisfy

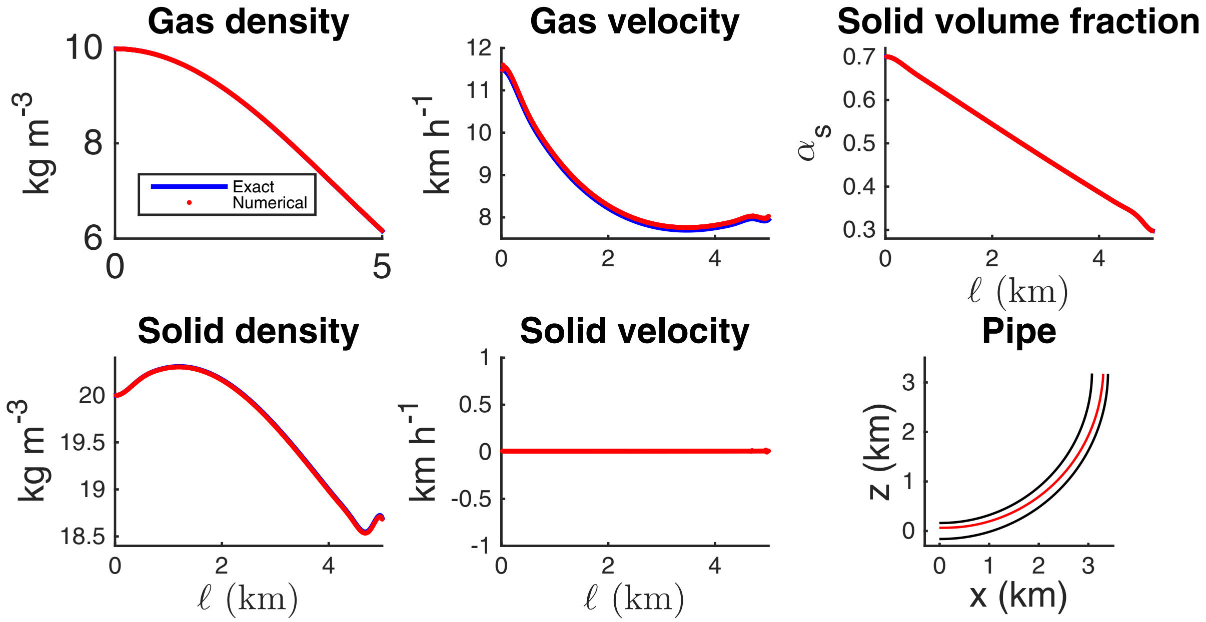

FIGURE 6. Exact (solid blue) and numerical (solid red) solutions at time $T = 30\,\mathrm{min}$ with initial conditions (4.3). The resolution here is $\Delta\ell = 10\,\mathrm{m}$ (500 gridpoints). *Top*: gas density (*left*), gas velocity (*middle*) and solid volume fraction (*right*). Bottom: solid density (*left*), solid velocity (*middle*) and a sagittal section illustration of the directional pipe, where the red curve represents the separation of the solid and gas phases (*right*).

stability properties such as non-negativity of the layer's depth, entropy inequalities and preservation of steady states.

Here we consider a vacuum problem, where the solid volume is very small in the left hand side and almost 1 in the right hand side of the pipe. This corresponds to a situation where the pipe is separated by a membrane and most of the cross-sectional area is occupied by the solid phase in the right hand side, with the opposite proportion in the left hand side. We expect that one of them pushes the other, developing shock, rarefaction and compaction waves in its time evolution. The challenge in this numerical test is the positivity-preserving property. The numerical scheme was constructed in a way that the solid- and gas- densities and volume fractions preserve positivity, adding stability to the solution in those situations. In the problem below, both gas and solid volume fractions are very small in certain regions of the domain.

The domain is $[0\,\mathrm{km}, 5\,\mathrm{km}]$, the ratio of gas constants are $\gamma = 1.4$ and $\gamma_s = 1.92$ and the gas and solid entropies are $\eta = 1\,\mathrm{Pa}$ and $\eta_s = 5\,\mathrm{Pa}$. The gravitational constant is $g = 9.81\,\mathrm{m\,s^{-2}}$. The pipe is horizontal ($\theta = 0$) and there is no interfacial friction ($F_{dg} = 0$). The stiffening pressure here is $p_o = 8.49\,\mathrm{Pa}$.

The initial conditions are given by

$$(\rho, u, \rho_s, u_s, \alpha_s) = \begin{cases} (10\,\mathrm{kg\,m^{-3}},\, 0\,\mathrm{km\,h^{-1}},\, 1\times10^{-1}\,\mathrm{kg\,m^{-3}},\, 0\,\mathrm{km\,h^{-1}},\, 0.01) & \text{if } \ell \le 5\,\mathrm{km}, \\[2ex] (2\times10^{-1}\,\mathrm{kg\,m^{-3}},\, 0\,\mathrm{km\,h^{-1}},\, 20\,\mathrm{kg\,m^{-3}},\, 0\,\mathrm{km\,h^{-1}},\, 0.95) & \text{otherwise.} \end{cases} \tag{4.4}$$

Figure 7 exhibits the numerical solution for the problem with the above initial conditions at time $T = 3\,\mathrm{min}$ and resolution $\Delta_\ell = 5\,\mathrm{m}$ (1000 gridpoints). We implement free (Neumann) boundary conditions. In practice, we extrapolate the data in the first/last cell to define the data in the ghost (boundary) cells. The gas density and gas velocity as functions of the pipe's arclength position are shown in the left and middle upper panels,

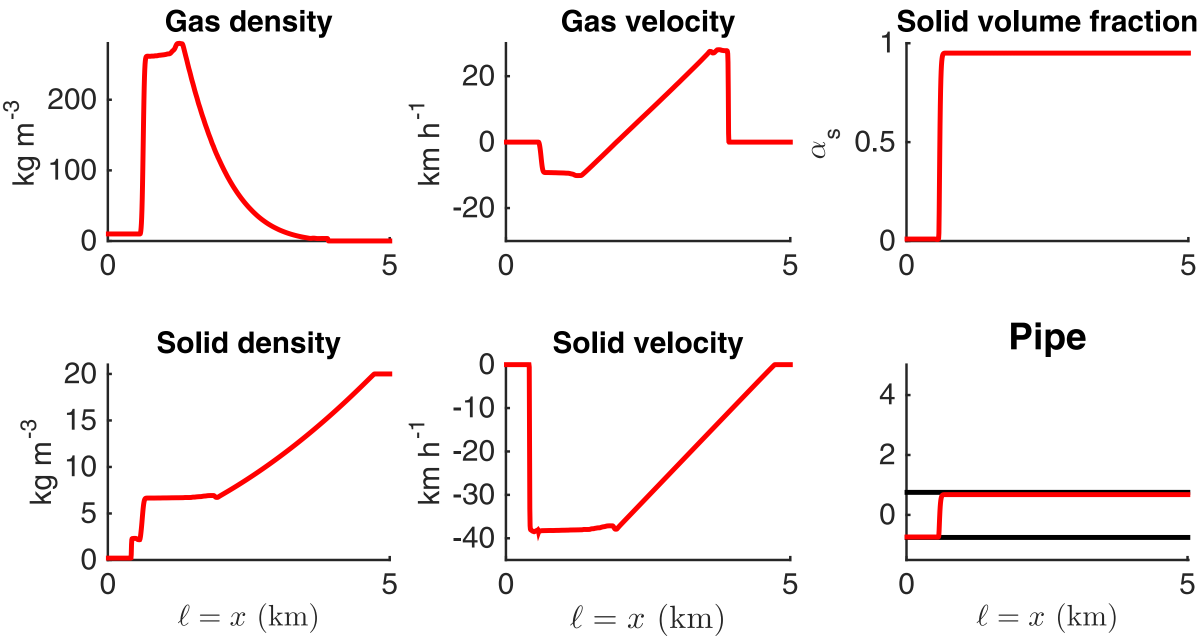

FIGURE 7. Numerical solutions to the problem with initial conditions (4.4) at time $T = 3\,\mathrm{min}$ and resolution $\Delta\ell = 5\,\mathrm{m}$ (1000 gridpoints). The plots follow the same order as in Figure 6.

whereas the bottom row shows the solid counterparts. In the right column we include the solid volume fraction (top right) and an illustration of the pipe with the sagittal sectional area (bottom right) separated by the area occupied by the solid (below) and gas (above) phases. In the solution one can observe a compaction wave that is visible in the solid volume fraction. The pipe does not have a given thickness and this illustration shows a proportion of the area occupied by each phase according to the volume fraction. In the solid phase we also identify a left shock wave followed by a compaction wave and a right rarefaction. In the gas phase we observe the compaction wave, followed by a left rarefaction wave and a right shock wave. We note that even though ρ, ρ_s, α, α_s are very small in different regions of the domain, their positivity is preserved and the numerical method is stable.

4.4. Accumulation of solids in deviated pipes

In this subsection, the geometry of the domain represents a deviated pipe. This scenario is common when considering directional drilling in wellbores. A deviated pipe represents the direction of a wellbore along some trajectory to a predetermined target. It is important to keep the wellbore contained within some prescribed limits relative to an inclination angle, horizontal excursion from the vertical or both. More details on definitions for directional drilling of a wellbore are shown in Chenevert *et al.* [3]. Numerical examples considering angles for the directional drilling are held in this subsection.

The polytropic exponents are $\gamma = 1.4$ and $\gamma_s = 1.92$ and the gas and solid entropies are $\eta = 2 \times 10^4\,\mathrm{Pa}$ and $\eta_s = 3.14 \times 10^3\,\mathrm{Pa}$. The stiffening pressure here is $p_o = 848.76\,\mathrm{Pa}$. The gravitational constant is $g = 9.81\,\mathrm{m\,s^{-2}}$. The angle at each arclength position in the pipe is given by

$$\theta(\ell) = 0.95\frac{\pi}{2}\left(\frac{\ell}{5\,\mathrm{km}}\right)^{1/5}.$$

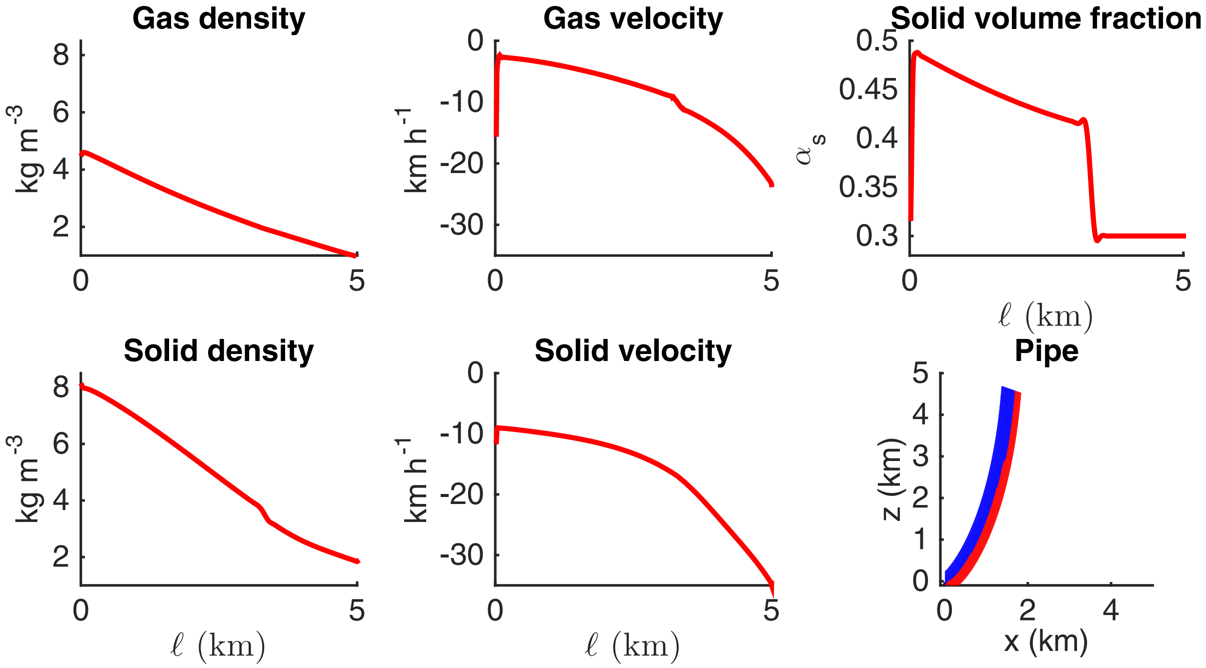

FIGURE 8. Numerical solution to the problem with initial conditions (4.5) at time $T = 30\,\mathrm{s}$ with resolution $\Delta\ell = 10\,\mathrm{m}$ (500 gridpoints). The plots show the same order as in Figure 6 except that the *bottom right panel* shows a sagittal section illustration of the pipe.

That is, the pipe is horizontal at the bottom and it becomes almost vertical near the surface. In this more realistic scenario and following [14], we consider an interfacial friction given by

$$F_{dg} = -\frac{3}{4}\frac{C_d}{d_p}\alpha_s \rho |u - u_s|(u - u_s).$$

The values of C_d and d_p are not relevant but only its ratio, which here is taken as $C_d/d_p = 1.5\,\mathrm{m}^{-1}$. The numerical solution is computed at time $T = 30\,\mathrm{s}$ and $T = 30\,\mathrm{min}$ with resolution $\Delta\ell = 10\,\mathrm{m}$ (500 gridpoints).

The domain here is $[0\,\mathrm{km}, 5\mathrm{km}]$, and the initial conditions are given by

$$(\rho, u, \rho_s, u_s, \alpha_s) = \begin{cases} \left(4.5\,\mathrm{kg\,m}^{-3},\ 4.5\,\mathrm{km\,h}^{-1},\ 8\,\mathrm{kg\,m}^{-3},\ 0.4\,\mathrm{km\,h}^{-1},\ 0.3\right) & \text{if } 0 \le \ell \le 2.5\,\mathrm{km} \\ \left(1\,\mathrm{kg\,m}^{-3},\ 1\,\mathrm{km\,h}^{-1},\ 2\,\mathrm{kg\,m}^{-3},\ 1.6\,\mathrm{km\,h}^{-1},\ 0.3\right) & \text{otherwise.} \end{cases} \tag{4.5}$$

Figure 8 shows the numerical solution for the problem at time $T = 30\,\mathrm{s}$. The gas density, gas velocity and solid volume fraction are shown in the upper panels, whereas the bottom row shows the solid density (*left*) and solid velocity (*middle*). We note that the solid volume fraction is a non-dimensional quantity between 0 and 1 and it represents the fraction of the solid phase in the duct. The bottom right panel shows a sagittal section of the pipe with red colors indicating the solid phase and blue colors identifying the gas component of the flow. The middle panels illustrate the speed for the gas and solid phases. Both velocities are negative, indicating that the fluid is falling towards the bottom of the pipe. Figure 9 shows the solution at time $T = 30\,\mathrm{min}$. The solution has reached a steady state of the second type in Proposition 2.2. The solid volume fraction is non-uniform, the solid velocity is very weak, and the gas moves upward, exiting the pipe. The gas passes through a bed of accumulated solid particles.

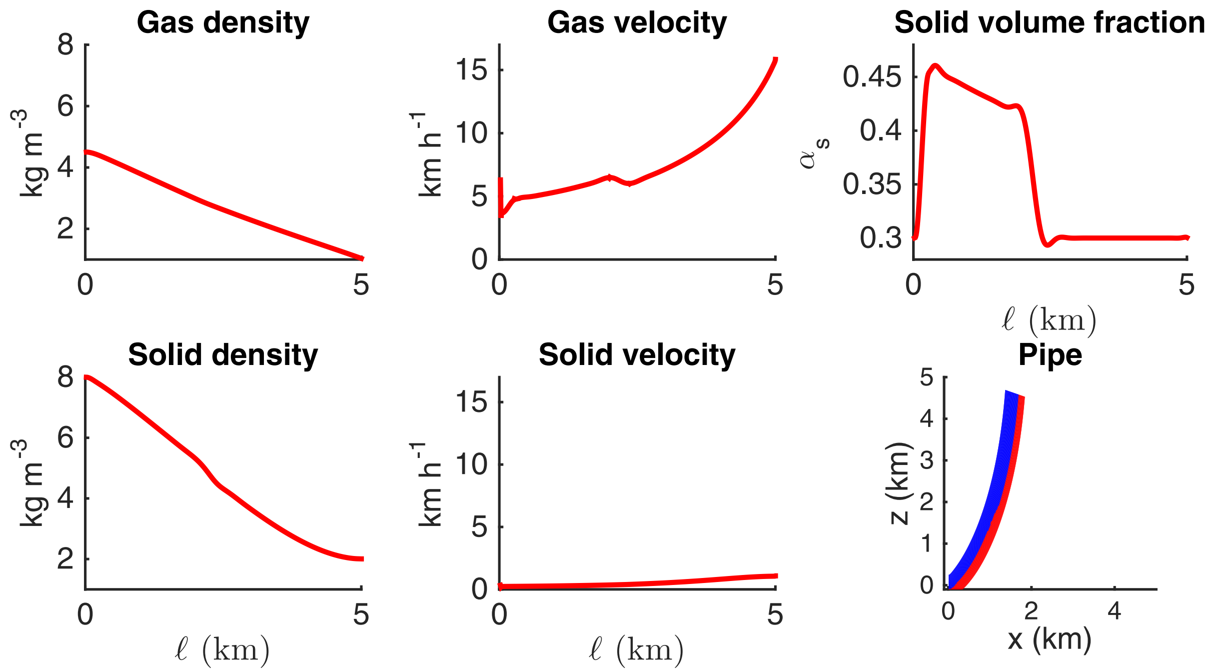

FIGURE 9. Numerical solution to the problem with initial conditions (4.5) at time $T = 30\,\text{min}$ with resolution $\Delta\ell = 10\,\text{m}$ (500 gridpoints). The plots show the same order as in Figure 6 except that the *bottom right panel* shows a sagittal section of the pipe.

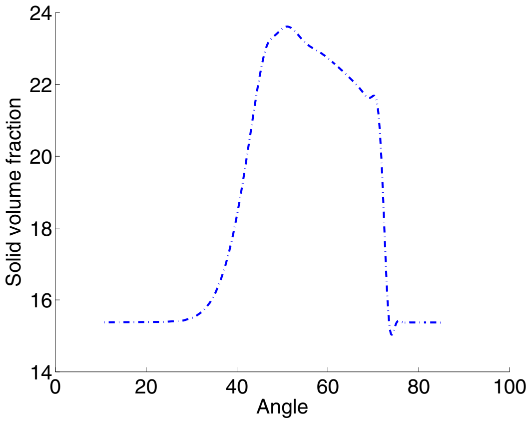

FIGURE 10. Solid volume fraction as a function of θ at time $T = 30\,\text{min}$. The initial conditions are given by (4.5). The resolution is $\Delta\ell = 10\,\text{m}$ (500 gridpoints).

As mentioned in the introduction, one of the potential applications of this model is in the analysis of accumulation of solids in certain locations of the pipe. As we have observed above, the steady states of the current model show a constant solid volume fraction with other invariants, or a non-uniform solid volume fraction with vanishing solid velocity. This second case corresponds to the phenomenon of accumulation of solids. Figure 10 shows the solid volume fraction as a function of angle at time $T = 30\,\text{min}$ where the initial conditions are taken from (4.5). We can observe a maximum accumulation of solids at about 50°, well within the range of critical

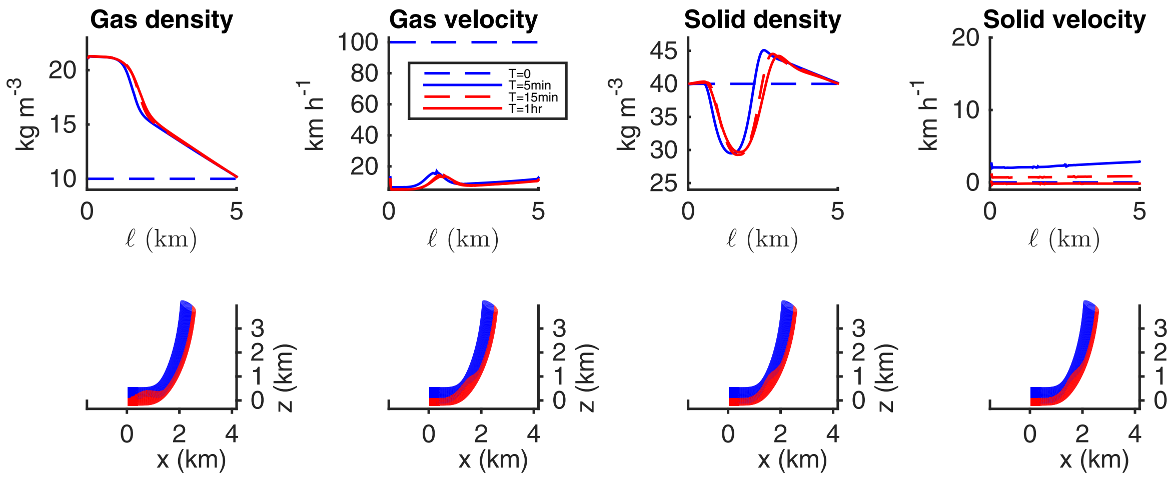

FIGURE 11. Numerical results for the initial conditions in (4.6), (4.7) and the boundary conditions described below with gas velocity at left boundary $u = 75\,\mathrm{km\,h^{-1}}$. *Top panel*: gas density, velocity, solid density and solid velocity at times $t = 0$ (dashed blue), 5 min (solid blue), 15 min (dashed red) and 1 hr (solid red) respectively. *Bottom panel*: three dimensional view of the pipe with solid accumulation in red.

angles for bed formation as mentioned in the introduction. Another approach in Lárez-Vázquez [24] studies this accumulation and other quantities in a different context. In such study, they analyze the efficiency of sand removal in deviated pipes with special interest in the relation between the particle bed as a function of the pipe's angle. Their algorithm is based on conservation of mass among other considerations, which differs from our approach using the two-phase flow model. Our results are in qualitative agreement with the preferred angle where the solids accumulate [24].

We repeat the simulation with the same parameters as in Figure 9 and initial conditions

$$(\rho, u, \rho_s, u_s) = \begin{cases} \left(10\,\mathrm{kg\,m^{-3}},\ 100\,\mathrm{km\,h^{-1}},\ 20\,\mathrm{kg\,m^{-3}},\ 0\,\mathrm{km\,h^{-1}}\right) & \text{if } \ell \le 2.5\,\mathrm{km}, \\[2ex] \left(10\,\mathrm{kg\,m^{-3}},\ 100\,\mathrm{km\,h^{-1}},\ 40\,\mathrm{kg\,m^{-3}},\ 0\,\mathrm{km\,h^{-1}}\right) & \text{otherwise}, \end{cases} \tag{4.6}$$

and initial volume fraction given by

$$\alpha_s = \begin{cases} 0.2 + \frac{1}{2}\cos\left(\frac{\pi}{2}\frac{\ell - 0.75\,\mathrm{km}}{0.75\,\mathrm{km}}\right)^2 & \text{if } 0\,\mathrm{km} \le \ell \le 1.5\,\mathrm{km}, \\ 0.2 & \text{otherwise}, \end{cases} \tag{4.7}$$

which corresponds to an accumulation of solids near the bottom of the pipe to be pushed by a discharge of gas at the bottom boundary. For that purpose, the boundary conditions at the left boundary consist of the following specifications. We extrapolate the gas/solid variables to the ghost cells at outflow ($u - c < 0$, $u_s - c_s < 0$) and impose $\rho_{s,\mathrm{in}} = 40\,\mathrm{kg\,m^{-3}}$, $\rho_{in} = 20\,\mathrm{kg\,m^{-3}}$ and $\alpha_{s,\mathrm{in}} = 0.2$ at inflow. At the surface, we impose $\rho_{s,\mathrm{out}} = 40\,\mathrm{kg\,m^{-3}}$, $\rho_{\mathrm{out}} = 10\,\mathrm{kg\,m^{-3}}$ and $\alpha_{s,\mathrm{out}} = 0.2$. The solid velocity is $0\,\mathrm{km\,h^{-1}}$ at inflow in both boundaries.

The numerical results are shown in Figures 11 and 12. Figure 11 considers a moderate gas discharge with a gas velocity of $75\,\mathrm{km\,h^{-1}}$ at the left boundary. After one hour, one can observe that the flow reaches a steady state with low solid velocity. The solid has accumulated at angles around 60°. We note however that increasing the gas discharge at the left boundary can push the solid up and clean the pipe. This can be verified in Figure 12

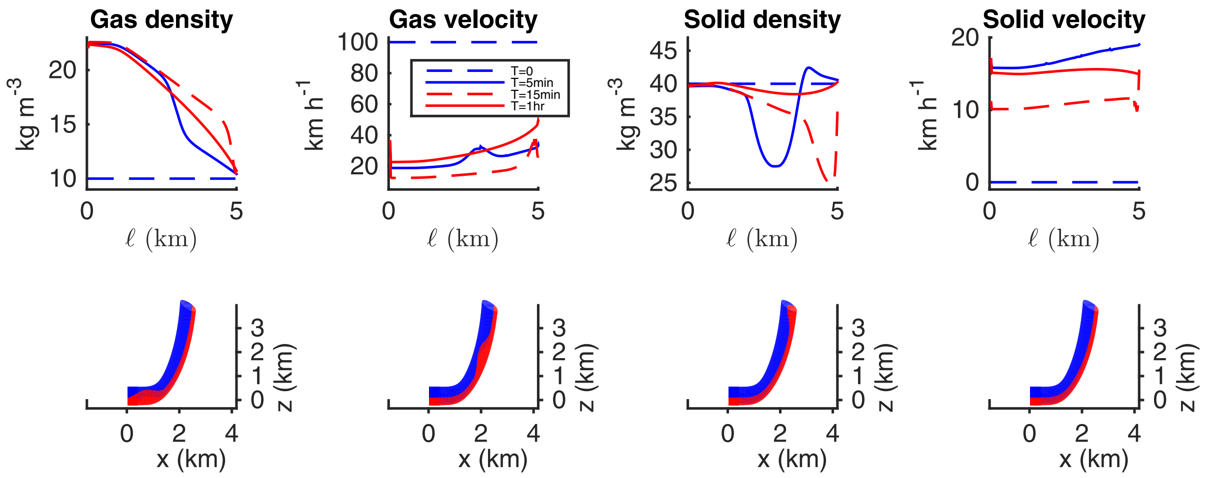

FIGURE 12. Same as in Figure 11, except that the gas velocity at left boundary is $u = 150\,\mathrm{km\,h^{-1}}$.

with a gas velocity of $150\,\mathrm{km\,h^{-1}}$ at the left boundary. Of course, in reality a gas discharge at the bottom is limited by the pump capacity.

5. CONCLUSIONS

In this work, an isentropic Baer-Nunziato model was considered and more physics that allows to analyze accumulation of solids in a deviated pipe were incorporated. The model considered a gas and a solid phase. It also considered friction between phases and gravity that depends on the pipe's angle. Spectral properties of the model were described and steady states were characterized by invariants. Furthermore, a positivity-preserving central-upwind scheme was constructed. A variety of numerical tests including Riemann problems and convergence to steady states show the merits of the scheme. An application to the study of accumulation of solids in deviated pipes was also shown.

APPENDIX A. A WELL-BALANCED PROPERTY

Among the steady states in Proposition 2.2 when $F_{dg} = 0$, one can recognize special steady states at rest in the absence of a solid phase satisfying

$$u_s = 0,\ \rho_s = \text{const.},\ \alpha_s = 0,\ u = 0 \text{ and } \frac{c^2}{\gamma - 1} + G = \text{const.} \tag{A.1}$$

Those steady states represent fluid at rest with no motion, no solid phase, and such that the gas pressure gradient is in balance with the integrated vertical component of gravity forces.

The source terms $\mathbf{S}(\mathbf{W}, \ell)$ in system (3.2) need to be discretized so that the numerical scheme can recognize the steady states at rest given in (A.1). In the following proposition we provide the details using the following notation for any quantity v

$$v_{j\pm\frac{1}{2}} = \frac{v^+_{j\pm\frac{1}{2}} + v^-_{j\pm\frac{1}{2}}}{2}. \tag{A.2}$$

Proposition A.1. *Let us assume the integrated gravity* $G = G(\ell) = g\int_{\ell_o}^{\ell} \sin(\theta(\ell))d\ell$ *is defined at the interfaces* $G_{j\pm\frac{1}{2}} = G(\ell_{j\pm\frac{1}{2}})$ *and the cell averages are* $G_j = (G_{j-\frac{1}{2}} + G_{j+\frac{1}{2}})/2$. *The quantity* $\frac{c^2}{\gamma-1} + G$ *is first reconstructed* *via* (3.9) *and* (3.10)*, which gives* $\rho^{\pm}_{j\pm\frac{1}{2}}$*,* $p^{\pm}_{j\pm\frac{1}{2}}$*. The other quantities to construct are* $\alpha\rho u$*,* $\alpha_s\rho_s u_s$*,* α_s *and* ρ_s*. The source terms* $\mathbf{S}(\mathbf{W},\ell)$ *in* (3.2) *are discretized as*

$$\frac{1}{\Delta\ell}\int_{\ell_{j-\frac{1}{2}}}^{\ell_{j+\frac{1}{2}}} p\partial_\ell \alpha_s d\ell \approx \bar{p}_j \frac{\alpha^-_{s,j+\frac{1}{2}} - \alpha^+_{j-\frac{1}{2}}}{\Delta\ell}, \tag{A.3}$$

$$\frac{1}{\Delta\ell}\int_{\ell_{j-\frac{1}{2}}}^{\ell_{j+\frac{1}{2}}} g\alpha\rho\sin(\theta(\ell))d\ell \approx g\bar{\alpha}_j\widehat{\rho}_j \frac{G_{j+\frac{1}{2}} - G_{j-\frac{1}{2}}}{\Delta\ell}, \tag{A.4}$$

where $\hat{\rho}_j$ *is a linearization satisfying*

$$\hat{\rho}_j \Delta\left(\frac{c^2}{\gamma-1}\right) = \Delta p. \tag{A.5}$$

The rest of the terms are approximated with regular averages as in (A.2)*. If the initial state satisfies* (A.1)*, then the numerical evolution given by* (3.13) *is independent of time.*

Proof. Le us assume that $\frac{c_j^2}{\gamma-1} + G_j$ is constant for all cells I_j. Then the reconstructions at the interfaces are trivial $\frac{c^2_{j\pm\frac{1}{2}}}{\gamma-1} + G_{j\pm\frac{1}{2}}$. This implies that $\rho^+_{j\pm\frac{1}{2}} = \rho^-_{j\pm\frac{1}{2}} = \rho_{j\pm\frac{1}{2}}$. As a result, the viscosity term in the numerical flux (3.7) vanishes. The flux difference is

$$\Delta(\alpha p) = \bar{p}\Delta\alpha + \bar{\alpha}\Delta p = -\bar{p}\Delta\alpha_s - \bar{\alpha}\hat{\rho}\left(-\frac{\Delta c^2}{\gamma-1}\right) = -\bar{p}\Delta\alpha_s - \bar{\alpha}\hat{\rho}\Delta G,$$

which concludes the proof. □

We note that the special reconstruction in the proposition may not respect the positivity of c^2. We can impose a correction to the reconstruction and ensure the positivity of $c^2_{j\pm\frac{1}{2}}$, which is the first step in the positivity-preserving property. The details are in Kurganov and Petrova [22].

We also note that none of the numerical tests we considered are the steady states at rest or small perturbations of them. Here we intend to show that it is possible to incorporate the well-balanced property in the numerical scheme if needed.

Appendix B. Solution to the Riemann problem

Here we consider the simplified case where the duct is horizontal ($\theta = 0$) and there is no friction between phases. Solutions to the Riemann problem consist of two single-phase compressible Euler sub-systems and an additional compaction wave, which carries changes in porosity and provides the means through which the two phases are coupled. Exact solutions to Riemann data may be obtained by starting from a given state, W_r for example, and build up a solution of a pre-determined configuration in the wave structure using known relationships that hold across the single-phase wavefronts and porosity jump. Those relationships are described case by case in the following subsections. For the sake of simplicity, let us assume the rarefaction wave is centered at $x = 0$.

Gas and solid rarefaction waves

Away from the compaction wave the term α_s is constant and the two Euler subsystems are decoupled. Across a gas rarefaction wave the solid phase remains constant and the gas phase can be obtained with the aid of the corresponding (non-trivial) Riemann invariant and the information of the eigenvalues, as follows

$$u \mp \frac{2c}{\gamma-1} = R = \text{Const.}, \quad u \pm c = \lambda_{1,2} = x/t.$$

Similarly, the solution across a solid rarefaction wave can be obtained by solving

$$u_s \mp \frac{2c_s}{\gamma - 1} = R_s = \text{Const.}, \quad u_s \pm c_s = \lambda_{3,4} = x/t.$$

Compaction wave

The compaction wave involves a jump in both gas and solid phases and couples the two subsystems. The Riemann invariants corresponding to this wave are [11, 28]

$$u_s,\ Q_{\mathrm{rel}} = \alpha\rho(u - u_s),\ H = \frac{1}{2}(u - u_s)^2 + \frac{c^2}{\gamma - 1},\ P = \phi p + \phi_s p_s + \phi\rho(u - u_s)^2,$$

which denote the solid velocity, momentum, enthalpy and the sum of of phase momenta fluxes as observed in the frame of reference of the compaction wave moving with speed u_s. It is a linearly degenerate field where $\lambda = u_s$ is constant across the wave. For a given right state, one computes the above Riemann invariants. If one fixes the left volume fraction $\alpha_{s,\ell}$, $\alpha_\ell = 1 - \alpha_{s,\ell}$, the left density is computed by solving

$$\frac{1}{2}Q_{\mathrm{rel}}^2 + \frac{\gamma\eta}{\gamma - 1}\alpha_\ell^2\rho_\ell^{\gamma+1} - H\alpha_\ell^2\rho_\ell^2 = 0,$$

and the rest of the variables can be computed from the density value.

Shock Waves

According to the Rankine-Hugoniot jump conditions, the solid phase is constant across a shock wave and the gas phase satisfies the relation

$$\begin{aligned} \Delta(\rho u) &= \sigma\Delta\rho, \\ \Delta(\rho u^2 + p) &= \sigma\Delta(\rho u), \end{aligned} \tag{B.1}$$

where σ is the speed of the shock wave and $\Delta(\cdot) = (\cdot)_r - (\cdot)_\ell$ is the difference between left and right states. Here we consider the general barotropic case where the pressure $p = p(\rho)$ is an explicit function of density. Combining the two equations in (B.1) we get

$$\Delta\rho\ \Delta p(\rho) = (\Delta(\rho u))^2 - \Delta(\rho u^2) = \rho_\ell\rho_r(\Delta u)^2.$$

Given ρ_r, u_r and fixing an appropriate left value ρ_ℓ, one can define

$$\tilde{c}^2 = \frac{\Delta(p(\rho))}{\Delta\rho}.$$

Therefore, the velocity for the right state is computed by the relation

$$\Delta u = \pm\frac{\tilde{c}}{\sqrt{\rho_\ell\rho_r}}\Delta\rho,$$

with a minus/plus sign for the left/right gas shock wave. The solid shock waves are computed analogously.

Acknowledgements. We thank the hospitality of International Laboratory for Human Genome Research, UNAM-Juriquillla where all of the co-authors were hosted since 2016. Research was supported in part by grants IA104517 to GHD, IN110917 to JXVH & a Conacyt (FORDECyT) postdoctoral grant number 265667 to UVG. Part of this work was done during the participation of the authors at the program Computational Issues in Oil Field Applications hosted by IPAM (UCLA) during the spring of 2017. The hospitality and generosity of IPAM and the organizers of the program is gratefully acknowledged. We also thank the reviewers for their thoughtful comments and help towards improving the paper.

References

[1] R. Abgrall and S. Karni, A comment on the computation of non-conservative products. *J. Comput. Phys.* **229** (2010) 2759–2763.

[2] N. Andrianov and G. Warnecke, On the solution to the Riemann problem for the compressible duct flow. *SIAM J. Appl. Math.* **64** (2004) 878–901.

[3] M.E. Chenevert, A.T. Bourgoyne, K.K. Millheim and F.S. Young, Applied drilling engineering, 48th edition. In: Society of Petroleum Engineers (1991).

[4] A. Bressan, Global solutions of systems of conservation laws by wave-front tracking. *J. Math. Anal. Appl.* **170** (1992) 414–432.

[5] L. Combe and J.M. Hérard, A finite volume algorithm to compute dense compressible gas-solid flows. *AIAA Journal* **37** (1997) 337–345.

[6] F. Coquel, J.M. Hérard and K. Saleh, A splitting method for the isentropic Baer-Nunziato two-phase flow model. In: CEMRACS'11: Multiscale Coupling of Complex Models in Scientific Computing In Vol. 38 of *ESAIM Proc.* EDP Sciences, Les Ulis (2012) 241–256.

[7] F. Coquel, J.M. Hérard, K. Saleh and N. Seguin. A class of two-fluid two-phase flow models. In: 42nd AIAA Fluid Dynamics Conference and Exhibit (2012) 3356.

[8] F. Coquel, J.M. Hérard, K. Saleh and N. Seguin, A robust entropy-satisfying finite volume scheme for the isentropic Baer-Nunziato model. *ESAIM: M2AN* **48** (2014) 165–206.

[9] D.H. Cuong and M.D. Thanh, Constructing a Godunov-type scheme for the model of a general fluid flow in a nozzle with variable cross-section. *Appl. Math. Comput.* **305** (2017) 136–160.

[10] G. Dal Maso, P.G. Lefloch and F. Murat, Definition and weak stability of nonconservative products. *J. Math. Pures Appl.* **74** (1995) 483–548.

[11] P. Embid and M. Baer, Mathematical analysis of a two-phase continuum mixture theory. *Contin. Mech. Thermodyn.* **4** (1992) 279–312.

[12] F.O. Farah, Directional well design, trajectory and survey calculations, with a case study in Fiale, Asal rift, Djibouti. Report 27, United Nations University, Geothermal Training Programe (2014).

[13] T. Flåtten, U.J.F. Aarsnes and O.M. Aamo, Review of two-phase flow models for control and estimation. *Annu. Rev. in Control* **42** (2016) 50–62.

[14] J.R. García-Cascales, J. Mulas-Pérez and H. Paillère, Extension of some numerical schemes to the analysis of gas and particle mixtures. *Int. J. Numer. Methods Fluids* **56** (2008) 845–875.

[15] P. García-Navarro and M.E. Vazquez-Cendon, On numerical treatment of the source in the shallow water equations. *Comput. Fluids* **29** (2000) 951–979.

[16] J. Glimm, Solutions in the large for nonlinear hyperbolic systems of equations. *Commun. Pure Appl. Math.* **18** (1965) 697–715.

[17] S. Gottlieb, C.W. Shu and E. Tadmor, Strong stability-preserving high-order time discretization methods. *SIAM Rev.* **43** (2001) 89–112.

[18] G. Hernandez-Duenas, A hybrid method to solve shallow water flows with horizontal density gradients. *J. Sci. Comput.* **73** (2017) 753–782.

[19] S. Karni, Hybrid multifluid algorithms. *SIAM J. Sci. Comput.* **17** (1996) 1019–1039.

[20] A. Kurganov, M. Prugger and T. Wu, Second-order fully discrete central-upwind scheme for two-dimensional hyperbolic systems of conservation laws. *SIAM J. Sci. Comput.* **39** (2017) A947–A965.

[21] A. Kurganov and G. Petrova, A second-order well-balanced positivity preserving central-upwind scheme for the Saint-Venant system. *Commun. Math. Sci.* **5** (2007) 133–160.

[22] A. Kurganov and G. Petrova, Central-upwind schemes for two-layer shallow water equations. *SIAM J. Sci. Comput.* **31** (2009) 1742–1773.

[23] A. Kurganov and E. Tadmor, New high-resolution central schemes for nonlinear conservation laws and convection-diffusion equations. *J. Comput. Phys.* **160** (2000) 241–282.

[24] R.E. Lárez-Vázquez, *Desarrollo de un modelo mecanístico para predecir la eficiencia de impieza de arena con tubería flexible en pozos inclinados.* Master's thesis, Universidad Autónoma de México (2005).

[25] P.G. LeFloch, Hyperbolic systems of conservation laws: The theory of classical and nonclassical shock waves. Lectures in Mathematics ETH Zürich. Birkhäuser Verlag, Basel (2002).

[26] P.G. LeFloch, Graph solutions of nonlinear hyperbolic systems. *J. Hyperbolic Differ. Equ.* **1** (2004) 643–689.

[27] R.J. LeVeque, Numerical methods for conservation laws. *Lectures in Mathematics ETH Zürich.* Birkhäuser Verlag, Basel (1990).

[28] C.A. Lowe, Two-phase shock-tube problems and numerical methods of solution. *J. Comput. Phys.* **204** (2005) 598–632.

[29] J.W. Nunziato and M.R. Baer, A two-phase mixture theory for the deflagration-to-detonation transition (ddt) in reactive granular materials. *Int. J. Multiphase Flow* **12** (1986) 861–889.

[30] T. Nazari, G. Hareland and J.J. Azar, Review of cuttings transport in directional well drilling: Systematic approach. In: *SPE Western Regional Meeting, 27–29 May, Anaheim, California, USA* (2010).

[31] I. Orozco-Castillo, *Modelo hidráulico para el transporte de sólidos en pozos altamente desviados*. Master's thesis, Facultad de Ingeniería UNAM (2014).

[32] C. Parés, Numerical methods for nonconservative hyperbolic systems: A theoretical framework. *SIAM J. Numer. Anal.* **44** (2006) 300–321.

[33] B. Perthame and C. Simeoni, A kinetic scheme for the Saint-Venant system with a source term. *Calcolo* **38** (2001) 201–231.

[34] J. Sanchez-Martinez, *Modelo hidráulico para la planeación de la perforación de pozos de alcance extendido en la cuenca terciaria de veracruz.* Master's thesis, Facultad de Ingeniería UNAM (2007).

[35] D.W. Schwendeman, C.W. Wahle and A.K. Kapila, The Riemann problem and a high-resolution Godunov method for a model of compressible two-phase flow. *J. Comput. Phys.* **212** (2006) 490–526.

[36] D. Serre, Systèmes de lois de conservation. I. Fondations. [Foundations]. Hyperbolicité, entropies, ondes de choc. [Hyperbolicity, entropies, shock waves]. Diderot Editeur, Paris (1996).

[37] M.D. Thanh, Exact solutions of a two-fluid model of two-phase compressible flows with gravity. *Nonlinear Anal. Real World Appl.* **13** (2012) 987–998.

[38] M.D. Thanh, Building fast well-balanced two-stage numerical schemes for a model of two-phase flows. *Commun. Nonlinear Sci. Numer. Simul.* **19** (2014) 1836–1858.

[39] M.D. Thanh, A phase decomposition approach and the Riemann problem for a model of two-phase flows. *J. Math. Anal. Appl.* **418** (2014) 569–594.

[40] M.D. Thanh, Well-balanced Roe-type numerical scheme for a model of two-phase compressible flows. *J. Korean Math. Soc.* **51** (2014) 163–187.

[41] M.D. Thanh and D.H. Cuong, Existence of solutions to the Riemann problem for a model of two-phase flows. *Electron. J. Differ. Equ.* (2015) 32–18.

[42] M.D. Thanh, D. Kröner and C. Chalons, A robust numerical method for approximating solutions of a model of two-phase flows and its properties. *Appl. Math. Comput.* **219** (2012) 320–344.

[43] M.D. Thanh, D. Kröner and N.T. Nam, Numerical approximation for a Baer-Nunziato model of two-phase flows. *Appl. Numer. Math.* **61** (2011) 702–721.

[44] P.H. Tomren, A.W. Iyoho and J.J. Azar, Experimental study of cuttings transport in directional wells. In: Society of Petroleum Engineers, Drilling Engineering (1986).

[45] B. van Leer, Towards the ultimate conservative difference scheme. V. A second-order sequel to Godunov's method. With an introduction by Ch. Hirsch, Commemoration of the 30th anniversary {of J. Comput. Phys.}. *J. Comput. Phys.* **32** (1979) 101–136. *J. Comput. Phys.* **135** (1997) 227–248.